Frontiers of Information Technology & Electronic Engineering
www.jzus.zju.edu.cn; engineering.cae.cn; www.springerlink.com
ISSN 2095-9184 (print); ISSN 2095-9230 (online)
E-mail: jzus@zju.edu.cn

***Review:***

# Advances in deep ultraviolet laser based high-resolution photoemission spectroscopy*

Zu-yan XU[1], Shen-jin ZHANG[†‡1], Xing-jiang ZHOU[2], Feng-feng ZHANG[1], Feng YANG[1], Zhi-min WANG[1], Nan ZONG[1], Guo-dong LIU[2], Lin ZHAO[2], Li YU[2], Chuang-tian CHEN[1], Xiao-yang WANG[1], Qin-jun PENG[3]

[1]*Key Laboratory of Function Crystal and Laser Technology, Technical Institute of Physics and Chemistry, Chinese Academy of Sciences, Beijing 100190, China*

[2]*National Laboratory for Superconductivity, Beijing National Laboratory for Condensed Matter Physics, Institute of Physics, Chinese Academy of Sciences, Beijing 100190, China*

[3]*Key Laboratory of Solid State Laser, Technical Institute of Physics and Chemistry, Chinese Academy of Sciences, Beijing 100190, China*

[†]E-mail: zhangshenjin@163.com

Received Nov. 24, 2018; Revision accepted May 28, 2019; Crosschecked July 12, 2019

**Abstract:** We briefly review recent results on photoemission spectroscopy based on the deep and vacuum ultraviolet diode pumped solid-state lasers which we have developed. Cascaded second harmonic generation with the nonlinear crystal $KBe_2BO_3F_2$ (KBBF) is used to generate deep ultraviolet and vacuum ultraviolet laser radiation, which complements traditional incoherent light sources such as gas discharge lamps and synchrotron radiation, and has greatly improved resolution with respect to energy, momentum, and spin of photoemission spectroscopy. Many new functions have been developed with the advantages of high photon energy, narrow linewidth, high photon flux density, and so on. These have led to the observation of various new phenomena and the amassment of new data in the fields of high temperature superconductivity, topological electronics, Fermi semi-metals, and so forth. These laser systems have revived the field of photoemission spectroscopy and provided a new platform in this frontier research field.

**Key words:** Deep and vacuum ultraviolet laser; Second harmonic generation; $KBe_2BO_3F_2$ nonlinear crystal; Photoelectron spectroscopy
https://doi.org/10.1631/FITEE.1800744 **CLC number:** O437

## 1 Introduction

Generally, light sources, especially those in the deep ultraviolet (DUV) and vacuum ultraviolet (VUV) ranges (both are collectively called DUV in this paper), with wavelengths from 250 to 185 nm and 185 to 100 nm, respectively, play a major role in photoemission spectroscopy, Raman spectroscopy, precise micromachining, and many other applications (Peng et al., 2018).

There are several sources of DUV light, including synchrotron radiation, gas discharges, excimer lasers, free electron lasers, high harmonic generation, four-wave mixing, and nonlinear frequency conversion (Cyranoski, 2009; Couprie, 2014). These can generally be classed as either noncoherent or coherent.

‡ Corresponding author
* Project supported by the National Development Project for Major Scientific Research Facility (No. ZDYZ2012-2) and the National Instrumentation Program (No. 2012YQ120048)
ORCID: Shen-jin ZHANG, http://orcid.org/0000-0002-3198-6971

Synchrotron radiation and gas discharge lamps are the most commonly used noncoherent DUV light sources (Greber et al., 1997; Xu et al., 2008). The former covers a wide wavelength range from 1 to 200 nm, and aroused great interest in earlier days. However, its several intrinsic disadvantages of low energy resolution (1–5 meV), low photon flux ($10^{10}$–$10^{12}$ photons/s), difficulty to focus, huge size, and high cost limit its range of application.

Gas discharge lamps have the advantages of continuous radiation, simple operation, and small volume, but the emission wavelengths are discrete because each excited gas can generate only specific wavelengths, such as 21.2 eV for He gas. Moreover, similar to synchrotron radiation, they have the same limitations of low energy resolution (about 1.2 meV), only one mode of operation, and low photon flux (less than $10^{14}$ photons/s).

High harmonic generation and four-wave mixing with a gas medium or metal vapor, respectively, can generate tunable DUV coherent radiation through the third-order nonlinear effect, but the output power energy and efficiency are very low.

Excimer lasers are one of the most widely used coherent light sources and are especially useful for immersion lithography (Grüner et al., 2007). Two main kinds, the 193 nm ArF and 157 nm $F_2$ pulsed lasers, can produce up to kilowatts of high power at 1 Hz–1 kHz repetition rates with nanosecond pulse widths. Unfortunately, an excimer laser has a poisonous gas medium, a limited number of wavelengths, a narrow tuning range, poor beam quality, poor stability, and a short lifetime, and only one gas fill is possible. Moreover, it is very difficult to control the spectral- and spatial-mode qualities of the excimer laser, meaning that it cannot meet the precision and practicality demands of the state-of-the-art scientific instruments.

The free electron laser has excellent characteristics, such as extremely wide wavelength tunability (extending down to X-rays) and high output power. However, its drawbacks include immature technology, complexity, large size, and high cost.

Another type of DUV laser is based on nonlinear frequency conversion. By sum-frequency mixing (SFM), several nonlinear crystals can be used to generate DUV light (Nagashima and Liu, 2001; Peng et al., 2018). For instance, DUV radiation at 172.7 nm has been generated with lithium triborate (LBO), and 166 nm with $KB_5O_8{\cdot}4H_2O$ ($KB_5$) (Petrov et al., 1998a, 1998b). Emission over a range of 170–180 nm from $Li_2B_4O_7$ ($LB_4$) and at 191.7 nm from $CsLiB_6O_{10}$ (CLBO) has been reported (Koch et al., 2016). With the $KBe_2BO_3F_2$ (KBBF) crystal, the shortest wavelength of 149.8 nm has been obtained by fifth harmonic generation of a Ti:sapphire laser (Nakazato et al., 2016). However, an SFM laser system is complex and inconvenient because it involves two different wavelength laser beams which require strict time synchronization, spatial superposition, and polarization matching. With quasi-phase matching, a 121 nm DUV laser has been realized in strontium tetraborate, $SrB_4O_7$ (SBO), but its intrinsic irregular behavior hinders its application (Trabs et al., 2016).

The disadvantages of the DUV light sources mentioned above have restricted their widespread application, especially for advanced scientific instruments that need very precise and user-friendly coherent light sources.

A more attractive way to produce DUV coherent light is based on cascaded second harmonic generation (SHG) with a diode-pumped solid-state laser (DPL) as the fundamental pump (called DUV-DPL in this paper). So far, SHG with a KBBF crystal is the best solution, being both precise and practical.

Compared to noncoherent light sources, the energy resolution of such diode-pumped lasers has been improved by about one order of magnitude, the photon flux by about five orders, and the photon flux density by about seven orders. They can operate at ns, ps, and fs pulse widths, and achieve a bulk effect of 10 nm detection depth, so they have great application prospects in the fields of physics, chemistry, material science, informatics, life science, and resource and environment research (Chen, 2004; Chen et al., 2009; Zhang SJ et al., 2014).

Our research team has developed a series of advanced DUV-DPL models that have already been incorporated in various analytic instruments. A typical example is the spectrometer used in high resolution angle-resolved photoelectron spectroscopy (ARPES), in which the major technical indicators (energy, momentum, and spin resolution) have been improved by several orders of magnitude, and many new functions have been developed.

In this paper we briefly review the characteristics of the DUV lasers developed by our research

team over more than 20 years and successfully employed in ARPES. The latest results obtained in the studies of high temperature superconductors, topological electronics, Fermi semiconductor metal materials, etc. will be reported.

## 2 Basic characteristics of deep and vacuum ultraviolet light source

The DPL has characteristics of good beam quality, widely tunable wavelength range, high output power, high efficiency, small beam diameter, and compact setup. However, the wavelength does not reach the DUV wavelength range and it is very difficult to develop the DUV wavelength with the stimulated emission effect. With multistage frequency conversion technology, the DUV laser can be emitted from nonlinear crystals. So far, it is the best solution for realizing DUV coherent light source, which can be classed as SFM and SHG methods. The SFM technology has harsh application conditions because of complex technology, poor stability, and practical difficulty.

The DUV-DPL has merits in application such as the following:

1. Precise control of parameters. The frequency domain, time domain, space domain, and polarization parameters can be designed and regulated precisely for various requirements. For instance, as far as the KBBF nonlinear crystal is concerned, its adjustable wavelength range is wide and continuously tunable. The widely tunable wavelength range is 170–232 nm. The theoretically shortest SHG wavelength limitation is 161 nm. The narrow linewidth may be at kHz–MHz levels. The operation mode may be a pulse repetition rate from several Hz to several GHz. The pulse width can be designed to be ns, ps, or fs. Moreover, the polarization can be easily adjustable with an arbitrary direction: linear, circular, or elliptical polarization and left- or right-handed.

2. Practical functions. It has the advantages of being compact, stable, and highly efficient with good beam quality and long life. The output power can be controlled from several μW to several hundred mW. This is greater than what is needed. It can also be stable over a long period. For example, the output power fluctuation is ±2.1% (root mean square) when the average power output is 4 mW at 177.3 nm over 2 h and 1 mW for 24 h. High energy resolution (better than 0.25 meV), high photon flux ($10^{14}$–$10^{15}$ photons/s), and high photon flux densities ($10^{19}$–$10^{20}$ photons/(s·cm$^2$)) can be realized. Moreover, the cost is relatively low. The fixed wavelength 177.3 nm and widely tunable 175–210 nm prototypes are about 0.8 m×0.5 m×0.5 m and 1.2 m×1 m×0.5 m, respectively (Peng et al., 2018).

### 2.1 KBBF nonlinear crystal prism-coupled device

The SHG matching wavelengths of typical nonlinear crystals are shown in Fig. 1 (Wang GL et al., 2008). So far, KBBF nonlinear crystal is the only one that can realize DUV-DPL through SHG.

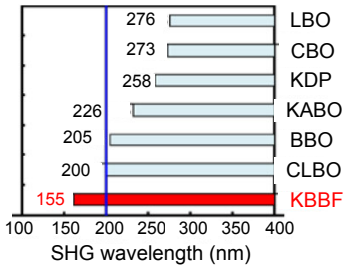


**Fig. 1 Second harmonic generation matching wavelengths for typical nonlinear crystals (reprinted from Wang GL et al. (2008), Copyright 2008, with permission from the Optical Society of America)**

However, its thickness does not exceed 4 mm because of the strong layering tendency along the *z* axis. Therefore, it cannot be cut along the phase-matched direction. Fig. 2a shows the phase-matched curve. To solve the layering effect problem we invented the special prism-coupled technique (patent), which has been granted by China, the United States, and Japan. In the KBBF prism-coupled device (KBBF-PCD), as shown in Fig. 2b, the KBBF nonlinear crystal is sandwiched between two prisms by optical contact, and they are then mechanically fixed together (Xu et al., 2001; Chen et al, 2004).

Considering the characteristics of the DUV laser and the KBBF nonlinear crystal, the two prism materials should meet these requirements:

1. The refractive index should be close to that of the KBBF nonlinear crystal.

2. Optical characteristic should be outstanding. Both the fundamental and DUV wavelengths should

be highly transparent in the two prisms.

3. Mechanical properties should be excellent and cutting should be relatively easy.

4. Physical performance should be excellent and the polishing surface should be of high flatness and high accuracy for good optical contact.

$CaF_2$ or $SiO_2$ is an ideal choice for the input prism and $CaF_2$ for the output prism with an apex angle of 68.6° (for a fixed wavelength 177.3 nm) or 60.0° (for a tunable wavelength 175–210 nm) by type-I phase-matching. The polarization direction of the input laser is along the *x* axis of the crystal, which has the maximum effective coefficient. The entity photo of the KBBF-PCD is shown in Fig. 3.

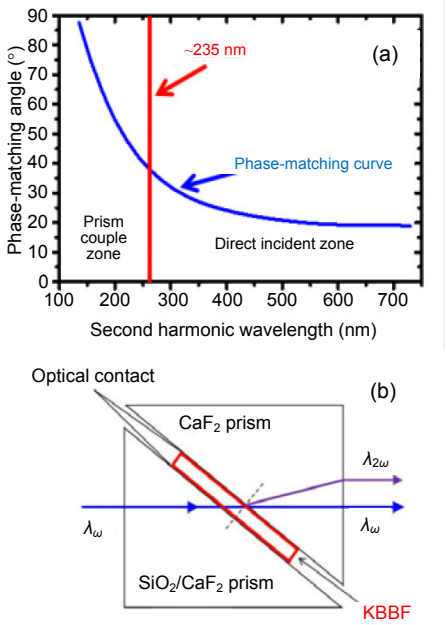


**Fig. 2 Second harmonic generation phase-matched curve of KBBF (a) and schematic of a KBBF-PCD (b) (reprinted from Peng et al. (2018), Copyright 2018, with permission from IEEE)**

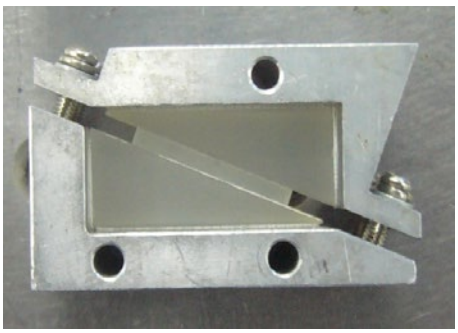

**Fig. 3 Photo of the KBBF-PCD entity**

A cooling system is used to precisely control the temperature of the crystal. The KBBF-PCD is fixed on a high resolution rotator with a minimum angular resolution of less than 0.2 mrad to precisely adjust the incident angle of fundamental laser for phase matching (Chen et al., 1996, 2008; Fujii et al., 2000; Lv et al., 2001; Kanai et al., 2009; Peng et al., 2018).

## 2.2 DUV-DPL based on KBBF-PCD

Over more than 20 years, we have developed a series of DUV-DPLs based on a series of KBBF-PCDs. It was first reported in 1996 and immediately attracted attention (Peng et al., 2018). In 2003, we achieved a ps laser at 177.3 nm with, later, 41 mW average power and a conversion efficiency of 0.54%. In 2007, emission over a range of ns 175–210 nm was realized. In 2008, fs 170–232 nm widely tunable wavelength was obtained with a 26.1% conversion efficiency, and the output power was scaled to 120 mW at 200 nm. In the same year, radiation of single pulse energy of 67 μJ was achieved with about 10% conversion efficiency, pulse repetition from 1 to 10 Hz, and about 20 ps pulse duration. The single pulse energy of the 355 nm laser is 600 μJ with a 1.5 mm beam diameter. The power density is 1.7 GW/cm$^2$ at 355 nm and 0.19 GW/cm$^2$ at 177.3 nm, which is higher than ns and ps lasers with higher pulse repetition rates by two orders of magnitude. The power density is so high that the KBBF-PCD is easily damaged, especially the optical contact surface and the output surface of $CaF_2$ prism. Enlarging the beam diameter size is an effective way to reduce the power density, but the aperture diameter of KBBF is limited. Then it is necessary to comprehensively consider the balance between reducing power density and enlarging the beam diameter. Meanwhile, the better optical quality and homogeneity of KBBF crystal is necessary because its beam diameter is several times larger than that of the other DUV-DPLs. In 2013, the ps range from 175 to 210 nm was generated with about 4 mW output power at 193 nm. The ns output power was 34.7 mW with a 10 kHz pulse repetition rate and about 0.82% energy conversion efficiency in 2009. The fundamental laser is a self-developed 4.2 W Nd:YAG laser at 355 nm with 49 ns pulse duration. In 2013, a narrow linewidth about 0.88 pm with the highest output power of 146.5 mW at 177.3 nm was obtained. The 355 nm fundamental laser was a 10 W

homemade ns frequency-tripled 1064 nm Nd:YAG laser. The linewidth was compressed by a specially designed quartz etalon. This result was selected as a research highlight by *Nature Photonics* in 2014.

In 2015 emission below 170 nm was demonstrated with a mode-locked ps 1342 nm Nd:$YVO_4$ laser at a 77 MHz pulse repetition rate. In 2016, an ns 164.9 nm laser was realized with mW level output power by the eighth harmonic generation based on a homemade 1319 nm Nd:YAG laser. As far as we know, it is the shortest DUV-DPL wavelength generated through cascaded SHG (Wang et al., 2008a, 2008b; Zhang HJ et al., 2008; Zhou Y et al., 2008; Li CM et al., 2009; Li FQ et al., 2012; Wang ZM et al., 2009; Yang F et al., 2009; Zhang X et al., 2009, 2011; Zhang Y et al., 2009; Zhang FF et al., 2012; Zhou C et al., 2012; Yang J et al., 2013; Zhang HJ et al., 2013; Xu Z et al., 2014a; Xu B et al., 2015; Peng et al., 2018).

In recent years, the DUV-DPL technology has made a spurt of progress. For instance, the wavelength has been shortened from 185 down to 164.9 nm, which is very close to the theoretical cutoff of about 161 nm of KBBF nonlinear crystal by SHG. It seems to be only a small amount of wavelength change, but it can bring about progress for instrument applications. As far as ARPES is concerned, the corresponding photon energy has been extended from about 6.2 eV (at which level only surface effects can be observed) to about 7.0 eV (at which level surface and bulk effects can be explored together), or even to about 7.5 eV (at which level almost the whole Fermi surface area can be characterized) (Dai et al., 2015, 2016). In recent years, the output power, SHG efficiency, and precise regulation technology of parameters have been increased. These benefit from not only the better optical quality of the fundamental laser and thicker KBBF nonlinear crystal, but also the harmonic generation techniques.

The key problem is how to improve further the performances of laser. This is determined not only by the improvement of KBBF-PCD and the harmonic process, but also by the regulation of the laser beam. For example, the damage threshold of KBBF-PCD is relatively low because of the low damage threshold of optical contact surface and $CaF_2$ prism, although the damage threshold of KBBF crystal is as high as 60 GW/cm$^2$.

For the optimum second harmonic generation progress, such as high efficiency conversion and good beam quality, the computational simulation of correlative parameters has been carried out for the expected output characteristics. Most factors are taken into consideration in theoretical calculation, for instance, the fundamental beam diameter in crystal, crystal length, birefringent effect, walk-off, spatial and temporal characteristics, and absorption and depletion of crystal. The simulation is appropriate for the ns and ps laser, including the optical conversion efficiency, pulse duration, spatial intensity profile, and beam quality. The results show that the walk-off angle of KBBF is rather large (about 54 mrad), so that the beam intensity profile and beam quality of DUV will be reduced nonlinearly when the crystal length increases. It indicates that the 3–5 mm effective crystal length and the 200–300 μm fundamental beam diameter in crystal are the optimum condition.

The temperature, incident angle, and environmental condition sensitivity of KBBF-PCD to the DUV generation process were considered in our past research. The thermodynamic characteristics of the KBBF crystal, prism, and cooling structure directly influence the frequency conversion process, and it is an important problem that cannot be ignored because the serious thermal effect will cause irreversible damage. The exit surface of the $CaF_2$ prism would break, and the optical contact surfaces separate because of the serious thermal effect during our past experiments. The non-negligible heat energy originates when the crystal and the two prisms intrinsically absorb the DUV and fundamental laser. The results show that the variation of the KBBF phase-matched angle with temperature is about 0.2′/°C, and the acceptable full-width-at-half-maximum angle tolerance is about 0.08°. These are so harsh that a small deviation from the normal working temperature or phase-matched angle will cause significant decrease of output power. It indicates that the high vacuum condition is more advantageous than the low vacuum one, and that the high purity nitrogen or helium condition is needed to obtain high output power and long-time stability. We also analyzed the pulse duration and the KBBF crystal third-order optical nonlinearity of the fs laser to describe the characteristics of the SHG process.

In past decades, several key technologies have been developed one by one. The DUV emission from

KBBF-PCD is very complex because of its particular sandwich structure that distinguishes it from the ordinary production method of visible or infrared lasers. The emission conditions are harsh because of the distinctive characteristics of KBBF crystal. Our results show that the fundamental laser with single mode ($M^2$<1.5) is more appropriate for generation of DUV than that with multimode ($M^2$>2). Furthermore, the laser with wavelength below 185 nm has strong absorption in air, so the emission, transmission, beam shaping, and measurement processes should be carried out in a vacuum chamber or high purity gas, such as nitrogen or helium. Many other steps are also considered for high transmission efficiency. For example, optical elements with low absorption, good quality reflective coatings with high damage thresholds, and a mechanical and electric controller with a smaller outgassing rate are chosen.

In this part, we will focus mainly on detailing our major research progress on the development of a series of DUV-DPL prototypes for ARPES.

### 2.2.1 DUV-DPL prototype with 177.3 nm fixed wavelength

The experimental schematic of the typical DUV-DPL with 177.3 nm fixed wavelength generated by the SHG of a 355 nm laser is as shown in Fig. 4 (Yang et al., 2013).

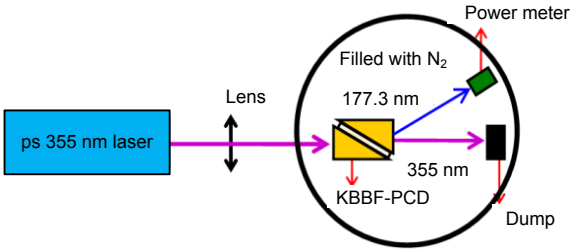


**Fig. 4 Experimental schematic of DUV-DPL with 177.3 nm fixed wavelength (reprinted from Yang et al. (2013), Copyright 2013, with permission from Elsevier)**

The measurements of 177.3 nm power as a function of incident 355 nm with different 355 nm beam diameters are shown in Fig. 5 (Yang F et al., 2010; Yang J et al., 2013). An average output power of 41 mW at 177.3 nm was obtained under 7.5 W at 355 nm with a conversion efficiency of 0.54%.

The relationship curves of calculated 177.3 nm versus 355 nm are shown in Fig. 6 with a 145 μm beam diameter (Yang et al., 2013). From the curves, we can see that the experimental results agree with the calculation results well when the pump power is low, but the deviation increases gradually when the pump power exceeds 4.3 W. It may be introduced by the phase mismatching of the KBBF crystal because its refractive index changes because of the thermal effect under high pump power. Therefore, it is necessary to improve further the effective cooling system of KBBF-PCD for higher DUV power.

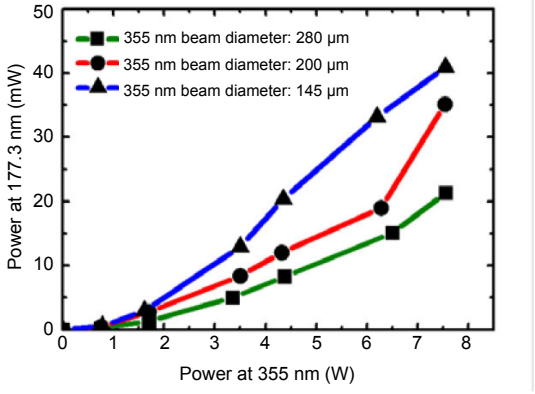


**Fig. 5 Output power at 177.3 nm versus that at 355 nm for different beam diameters (reprinted from Yang et al. (2013), Copyright 2013, with permission from Elsevier)**

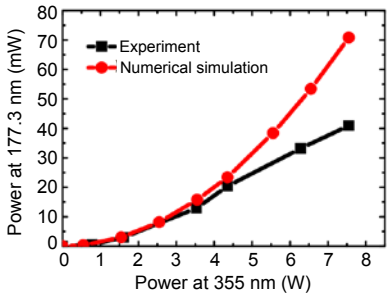


**Fig. 6 Calculation and experimental results at 177.3 nm versus 355 nm power with a 145 μm beam diameter (reprinted from Yang et al. (2013), Copyright 2013, with permission from Elsevier)**

After KBBF-PCD reaches thermal equilibrium, the stabilities of 177.3 nm output power and 355 nm input power are as shown in Fig. 7 (Yang et al., 2013). The fluctuations are about ±1.04% based on the key techniques we developed.

The fundamental pump source is a linear polarization Nd:$YVO_4$ laser with the $W$ level at 355 nm, 80 MHz pulse repetition rate, about 15 ps pulse

duration, and $M^2$<1.2 beam quality. For a normal incidence beam of 355 nm, its refractive angle inside the KBBF crystal is equivalent to a 64.5° phase-matched angle. The crystal thickness is 2.1 mm, corresponding to an optical path length of about 4.8 mm. The entity photo of the fixed wavelength ps MHz 177.3 nm prototype is shown in Fig. 8.

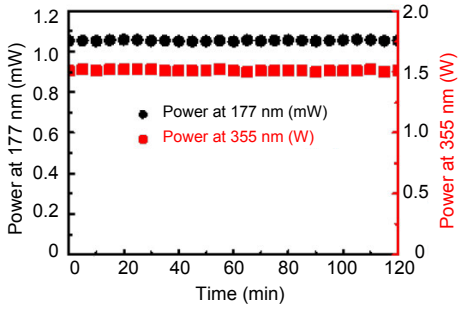


**Fig. 7 Power stabilities at 177.3 nm and 355 nm (reprinted from Yang et al. (2013), Copyright 2013, with permission from Elsevier)**

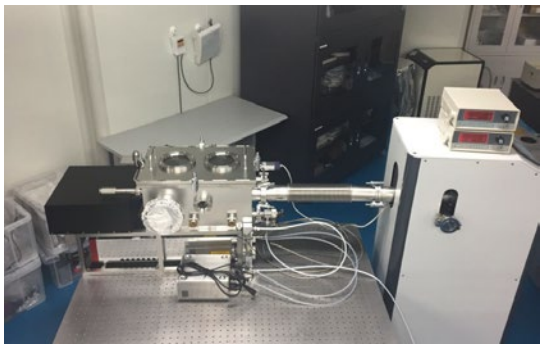

**Fig. 8 Photo of the DUV-DPL prototype with 177.3 nm fixed wavelength**

2.2.2 DUV-DPL prototype with arbitrarily adjustable polarizations

For some applications, such as ARPES, the adjustable polarizations are more important than the output power. The tunable polarizations are necessary for the photoemission matrix element effect and disentangle the orbital characteristics of the energy bands. The circular polarizations can be used to study magnetism or test time-reversal symmetry breaking. The scheme diagram of the ps 177.3 nm DUV-DPL with adjustable polarizations is shown in Fig. 9 (Zhang FF et al., 2012, 2013).

The pulse repetition rate of the 355 nm fundamental laser is 120 MHz with an about 22 ps pulse duration, which is the third harmonic of a 1064 nm laser. The thickness along the $z$ axis of type-I phase-matched KBBF crystal is 1.78 mm and a lens is used to focus the 355 nm laser beam into KBBF-PCD. The generated 177.3 nm laser in the first hermetical chamber is transmitted into the second hermetical chamber for beam shaping and adjustment. Both hermetical chambers are filled with pure nitrogen (>99.999%) at $1\times10^5$ Pa. In the second chamber, the 177.3 nm laser is collimated by a $CaF_2$ lens.

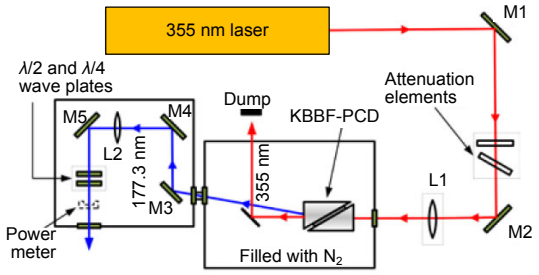


**Fig. 9 Schematic of 177.3 nm DUV-DPL with arbitrarily adjustable polarizations (reprinted from Zhang FF et al. (2012), Copyright 2012, with permission from the Chinese Physical Society and IOP Publishing Ltd.)**

Fig. 10 shows the azimuth angle $\alpha$ between the optical axis of the wave plate and the 177.3 nm polarization direction (Zhang FF et al., 2012). We can obtain easily any desired polarization state by rotating a $\lambda/4$ or $\lambda/2$ wave plate of 177.3 nm. The linearly polarized laser can be adjusted into a right/left-handed circularly or elliptically polarized laser by a $\lambda/4$ wave plate, and linear polarization with an arbitrary direction can be performed by rotating a $\lambda/2$ wave plate.

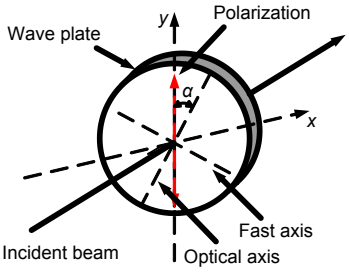


**Fig. 10 Azimuth angle $\alpha$ between the optical axis of the wave plate and the polarization direction of 177.3 nm (reprinted from Zhang FF et al. (2012), Copyright 2012, with permission from the Chinese Physical Society and IOP Publishing Ltd.)**

Polarization of 177.3 nm under various azimuth angles is given in Table 1. There is about 15% loss introduced by the $\lambda/4$ or $\lambda/2$ wave plate because there is no antireflection coating on the optical surface. The two wave plates are installed on an electric stepping motor with an angular resolution of 0.2 mrad to be arbitrarily rotated.

Fig. 11 shows the experimental power dependence at 177.3 nm versus 355 nm for two given polarization states, *s* and $\sigma^+$ polarizations.

**Table 1 Polarization of 177.3 nm laser under various azimuth angles**

| Rotation angle | Polarization | |
|---|---|---|
| | $\lambda/4$ wave plate | $\lambda/2$ wave plate |
| 0 | *p* | *p* |
| π/4 | $\sigma^-$ | *s* |
| 3π/4 | $\sigma^+$ | *s* |
| π/2, π | *p* | *p* |
| Others | Elliptical | Linear |

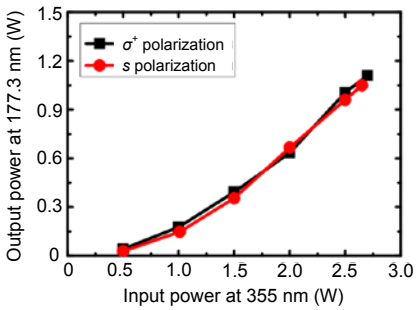


**Fig. 11 Power dependence at 177.3 nm versus 355 nm for *s* and $\sigma^+$ polarized lights (reprinted from Zhang FF et al. (2012), Copyright 2012, with permission from the Chinese Physical Society and IOP Publishing Ltd.)**

The power stability of the 1.1 mW *p*-polarization 177.3 nm laser over 1 h was measured experimentally with about ±1% fluctuation as shown in Fig. 12 (Zhang FF et al., 2012).

Fig. 13 shows the entity photo of the DUV-DPL prototype with arbitrarily adjustable polarizations (Zhang FF et al., 2012).

2.2.3 DUV-DPL prototype with an adjustable pulse repetition rate

Fig. 14 shows the experimental setup, and the fundamental pump source is a mode-locked frequency-tripled Nd:$YVO_4$ 355 nm laser with the adjustable pulse repetition rate from 200 kHz to 1 MHz and linewidth of 25 pm (Xu et al., 2014a, 2014b).

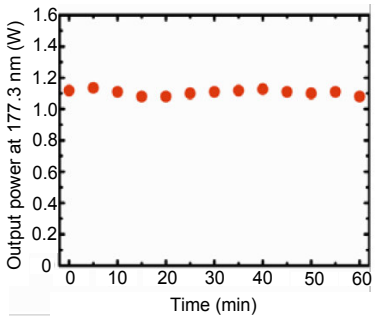


**Fig. 12 Stability measurement at *p*-polarized 177.3 nm (reprinted from Zhang FF et al. (2012), Copyright 2012, with permission from the Chinese Physical Society and IOP Publishing Ltd.)**

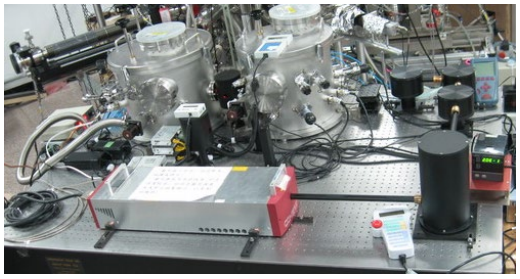

**Fig. 13 Photo of the 177.3 nm prototype with arbitrarily adjustable polarizations**

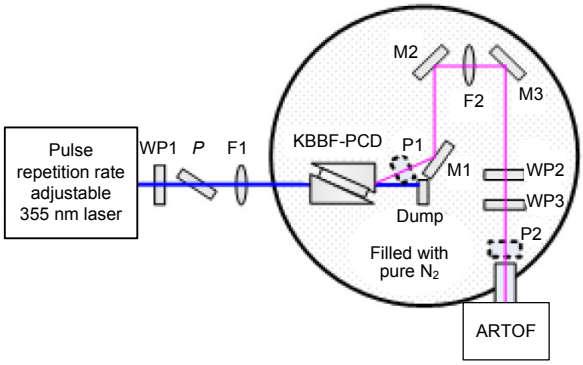


**Fig. 14 Experimental setup for the DUV-DPL with an adjustable pulse repetition rate (reprinted from Xu et al. (2014a), Copyright 2014, with permission from Springer)**

A $\lambda/2$ wave plate and a linear polarizer at 355 nm are used together to adjust the pump power to meet the experimental need.

The thickness of KBBF crystal is 1.35 mm and two $\lambda/4$ and $\lambda/2$ wave plates are used to adjust the polarizations of DUV. The output power at 177.3 nm versus that at 355 nm at different pulse repetition rates is shown in Fig. 15 (Xu et al., 2014a).

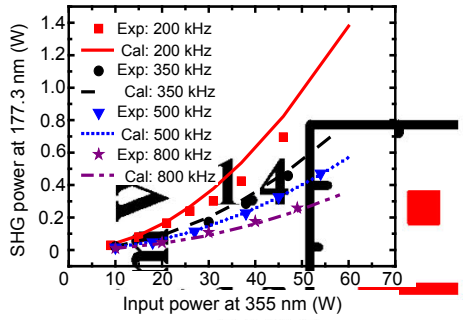


**Fig. 15 Measured and calculated 177.3 nm power versus 355 nm power at different pulse repetition rates (reprinted from Xu et al. (2014a), Copyright 2014, with permission from Springer)**

The experimental stability of 177.3 nm was monitored over 2 h under a 355 nm pump power of 25 mW, as shown in Fig. 16 (Xu et al., 2014a).

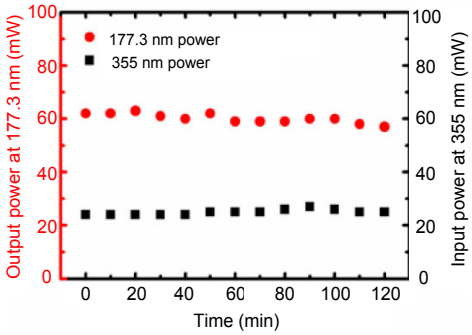


**Fig. 16 Stability curve at 177.3 nm and 355 nm with a 350 kHz pulse repetition rate (reprinted from Xu et al. (2014a), Copyright 2014, with permission from Springer)**

The 177.3 nm power was about 60 μW with vertical polarization and at the 350 kHz pulse repetition rate. Fig. 17 shows the entity photo of the DUV-DPL prototype with an adjustable pulse repetition rate.

### 2.2.4 DUV-DPL prototype with shorter wavelength

The wavelengths mentioned above are larger than 170 nm. The lasers whose photon energies are higher than 7.3 eV (170 nm) have major application in many scientific fields. For instance, the ARPES based on higher photon energy DUV-DPL, such as 7.5 eV (165 nm), can work on some materials with small lattice constants and a larger Brillouin zone, and reach the important (π, 0) antinodal region of high $T_c$ superconductors and other transition metal oxides.

**Fig. 17 Entity photo of the DUV-DPL prototype with an adjustable pulse repetition rate**

There are many difficulties in generating smaller wavelengths due to the fact that the conversion efficiency of KBBF is much lower and the absorption loss of the crystal and $CaF_2$ prism is more intense when the wavelength is smaller. Fig. 18 shows the transmittance curve of the KBBF crystal with 0.67 mm thickness and its corresponding absorption coefficient (Dai et al., 2015).

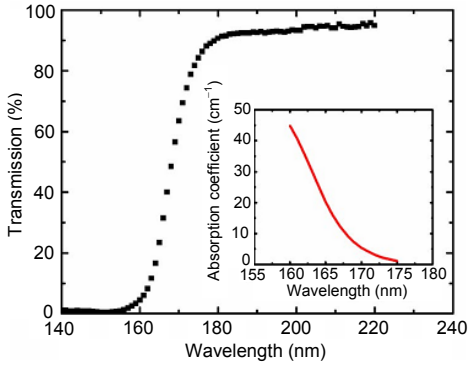


**Fig. 18 Transmittance and absorption coefficients of 0.67 mm thick KBBF crystal (reprinted from Dai et al. (2015), Copyright 2015, with permission from the Optical Society of America)**

As we can see from the two curves, there is almost no absorption when the wavelength is above 180 nm except for the Fresnel loss, and the transmission decreases sharply below 180 nm with about 46.8% at 167.75 nm, which corresponds to an about 10 $cm^{-1}$ absorption coefficient. In fact, work has seldom been reported on DUV-DPL below 170 nm by SHG. In this part, we will introduce a ps 167.75 nm DUV-DPL by eighth harmonic generation (EHG) from a 1342 nm laser.

In our experiment, the fundamental laser is a 17 W homemade *p*-polarized mode-locked Nd:$YVO_4$ laser with a 77 MHz pulse repetition rate and a 24 ps pulse duration.

The 167.75 nm laser is obtained by the twice cascaded SHG in two LBO crystals and finally EHG with KBBF crystal, as shown in Fig. 19 (Dai et al., 2015).

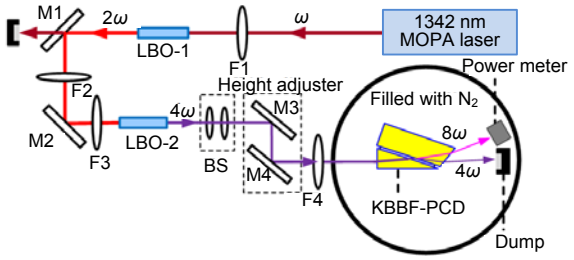


**Fig. 19 Schematic for generating ps DUV 167.75 nm laser (reprinted from Dai et al. (2015), Copyright 2015, with permission from the Optical Society of America)**

The maximum output power at 335.5 nm is 0.63 W with a pulse duration of 15.4 ps and beam quality of $M^2$ about 1.3.

A specially designed KBBF-PCD was invented to satisfy the type-I phase-matched condition of emitting 167.75 nm laser, as shown in Fig. 20 (Dai et al., 2015).

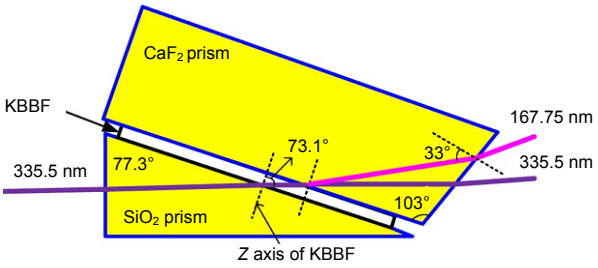


**Fig. 20 A specially designed structure of KBBF-PCD at 167.75 nm (reprinted from Dai et al. (2015), Copyright 2015, with permission from the Optical Society of America)**

A KBBF crystal is sandwiched between a right angle $SiO_2$ prism and a trapezoid $CaF_2$ prism with apex angles of 77.3° and 103°, respectively. The 0.6 mm thick KBBF crystal corresponds to 2.1 mm effective length. The structure of the trapezoid rear $CaF_2$ prism is specially designed for a 167.75 nm laser with a 33° incident angle on the output surface, which is the Brewster angle of the $CaF_2$/air interface and results in a Fresnel loss of about zero. The entity photo of the specially designed KBBF-PCD prototype for 167.75 nm is shown in Fig. 21.

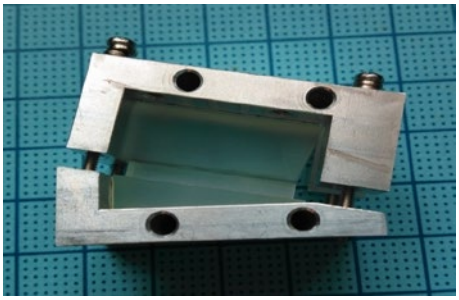

**Fig. 21 Photo of specially designed KBBF-PCD for a shorter wavelength**

The conversion efficiency increases by about 4% over that with the traditional device. The 73.1° refractive angle of 335.5 nm inside the KBBF crystal is the phase-matched angle to generate efficiently a 167.75 nm laser when the incident angle is about 1.8°. The polarization direction of the input 335.5 nm laser is along the *y* axis of the crystal, which allows a maximum effective coefficient of 0.14 pm/V.

The 65 μW output power at 167.75 nm was measured. Fig. 22 shows the entity photo of the 167.75 nm DUV-DPL prototype.

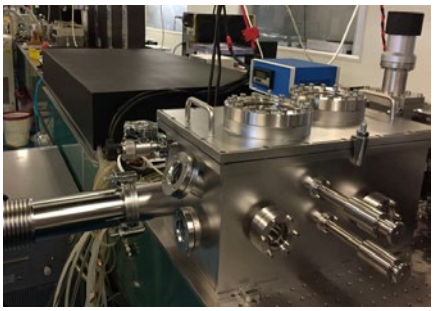

**Fig. 22 Entity photo of the 167.75 nm DUV-DPL prototype**

2.2.5 DUV-DPL prototype with widely tunable wavelength

An ARPES with tunable wavelengths is preferable and makes it possible to clarify the final state effect of the photoelectron, the overall band structure, and the three-dimensional (3D) dispersion curve in the momentum space.

In this part, we present a ps 80 MHz DUV-DPL with wavelength widely tunable from 175 to 210 nm, which has high pulse repetition rate, high energy resolution, and low space charge effect for ARPES.

It is a fourth harmonic generation of a Ti:sapphire laser through two stages of second harmonic generation. The experimental schematic layout is shown as Fig. 23. The fundamental Ti:sapphire laser is a linear polarization, mode-locked laser with wavelength tunable from 700 to 840 nm, about 2 ps pulse duration, and 80 MHz pulse repetition rate. The highest output power is 2.8 W at 772 nm and the output power in the whole range exceeds 2 W.

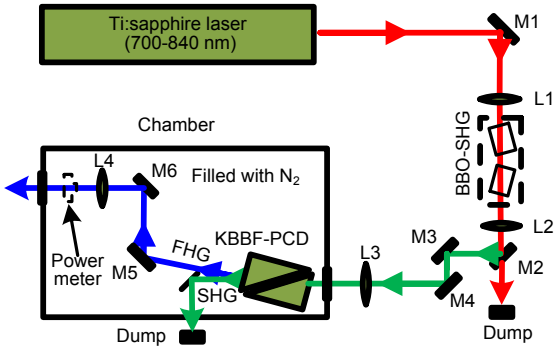


**Fig. 23 Experimental scheme for DUV-DPL with widely tunable wavelengths (reprinted from Zhang HJ et al. (2013), Copyright 2013, with permission from the Chinese Physical Society and IOP Publishing Ltd.)**

The walk-off angle of the β-$BaB_2O_4$ (BBO) crystal is rather large (about 85 mrad), so two BBO crystals are usually necessary for walk-off compensation and high output power during the process of producing a tunable wavelength from 350 to 420 nm. This technology also overcomes the difficulties by providing (1) higher conversion efficiency and better beam quality and (2) complete walk-off compensation to maintain the beam transmission along the same beam direction while the wavelength is adjusted.

The walk-off compensation specially designed is composed of two "twin" BBO crystals that are identically cut and type-I phase-matched. The dimensions of both BBO crystals are 8 mm×4 mm×6 mm, and the 8 mm side is used as the tuning side with 6 mm as the length. The BBO crystals are cut at $\theta$=30.8°, which is a mean value of the phase-matched angles of 33.7° and 27.9° for frequency doubling at 700 and 840 nm, respectively. The two BBO crystals are placed on a self-developed highly precise dual-axis rotation with a sophisticated reverse cascade walk-off compensation mechanical device. The angles of two BBO crystals can be adjusted by a knob with high accuracy and synchronization. With the two "twin" BBO crystals walk-off compensation and precise reverse cascade mechanical device, the beam quality of SHG is improved, and the walk-off of the beam pointing due to frequency tuning can be compensated, which is beneficial to the fourth harmonic generation (FHG). The 700 and 840 nm lasers are focused by a lens and the focus spot is in the middle of the two BBO crystals. The 350–420 nm laser is separated from the fundamental laser by three dichroic splitting mirrors and collimated by a lens.

The second harmonic laser is focused into a KBBF-PCD through a plane-convex lens, and the type-I phase-matched condition is satisfied to generate the 175–210 nm wavelength by SHG. The dimension of the KBBF crystal was 6 mm×20 mm×1.45 mm (where 1.45 mm was the thickness along the $z$ axis), and the apex angle of each prism was 60°, which corresponds to the phase-matched angle of 374 to 187 nm under the condition of normal incidence. The device is held on a rotator with high angular resolution of less than 0.2 mrad to adjust its phase-matched angles for different wavelengths from 350 to 420 nm. Two mirrors were used to align the 175–210 nm wavelength. Finally, a $CaF_2$ lens is placed to collimate the widely tunable DUV laser.

The output power of 1.1 W at 386 nm was obtained with a conversion efficiency of 40%. The $M^2$ beam quality factor of the horizontal axis and the vertical axis are $M_x^2$=1.80 and $M_y^2$=1.10, respectively. The $y$ direction beam quality is better than that in the $x$ direction. The main reason for this is the difference of acceptance angles for frequency doubling between two directions.

Fig. 24 shows the output power of SHG and FHG during the tunable wavelength range (Zhang HJ et al., 2013). The output powers of the FHG exceed 0.15 mW in the entire tunable range, and the highest power of FHG is 3.72 mW at 193 nm.

We tested the power stability of SHG and FHG at 350 and 175 nm, 386 and 193 nm, and 420 and 210 nm over 120 min (Fig. 25) (Zhang WT et al., 2013).

The entity photo of the DUV-DPL prototype with the ps 175–210 nm widely tunable wavelength is shown in Fig. 26. So far, we have developed the widely tunable ns, ps, and fs DUV-DPLs.

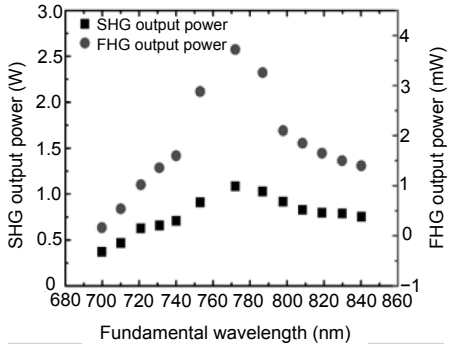


**Fig. 24 Output power of SHG and FHG as a function of the fundamental wavelength (reprinted from Zhang WT et al. (2013), Copyright 2013, with permission from the Chinese Physical Society and IOP Publishing Ltd.)**

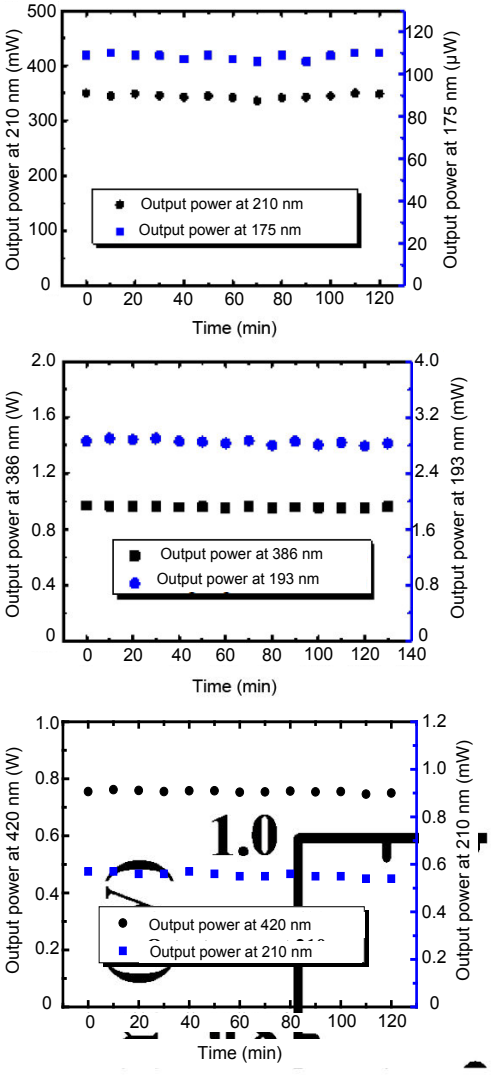


**Fig. 25 Stability curves of SHG and FHG power (reprinted from Zhang FF et al. (2013), Copyright 2013, with permission from the Chinese Physical Society and IOP Publishing Ltd.)**

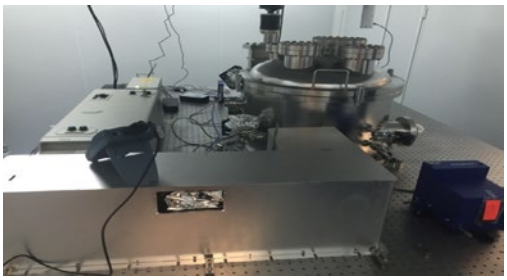

**Fig. 26 Entity photo of ps 175–210 nm widely tunable wavelength DUV-DPL prototype**

## 3 ARPES based on deep or vacuum ultraviolet with KBBF-PCD

Advanced materials, including correlated electron system and complex materials, magnetic materials, spintronics materials, and nanostructure and nanometer materials, are greatly active frontiers in modern condensed matter physics. On one hand, the application of these materials will have a direct and great impact on energy, information, environment, and other fields closely related to the national economy and people's lives. On the other hand, these new materials and new physical phenomena have provided opportunities for new scientific breakthroughs. For example, high-temperature superconductivity has been studied for more than 20 years since it was discovered, but the mechanism leading to high-temperature superconductivity is still unclear. This has become one of the most important physical problems in condensed matter physics research (Hüfner, 1995, 2003; Dagotto, 2005; Mai, 2013).

Photoelectron spectroscopy (PES) is the most direct and powerful experimental method for studying the microscopic electronic structures of advanced materials, such as high-temperature superconductors. It is necessary to understand the electronic structure of materials first to understand, control, and use the numerous novel physical phenomena in advanced materials. If we want to fully describe the state of electrons in materials, it is necessary to obtain three basic parameters: energy (E), momentum (M), and rotation (R). PES technology can be used to measure these parameters directly, so it is in an outstanding position in experimental research and theoretical development of strongly correlated electronic systems and other advanced materials.

Thus, PES technology has received extensive attention. It has made rapid progress because of the continuous improvement of the light and the introduction of advanced electronic detection technology. Every significant improvement of experimental methods will lead to the discovery of new phenomena in turn. The relationship of interdependence and promotion between instrument development and scientific deepening is particularly obvious, especially in PES technology.

### 3.1 Basic knowledge of ARPES

#### 3.1.1 Fundamental principles

The PES technique is based on the photoelectric effect, which is a quantum phenomenon discovered by Hertz in 1887. It was theoretically explained by Einstein in 1905 by introducing the quantum nature of light in "On the heuristic viewpoint concerning the production and transformation of light" (Hertz, 1887; Einstein, 1905; Nordling et al., 1957; Smith et al., 1974; Nomura et al., 2001; Damascelli et al., 2003).

The basic principle of PES is very simple. When a sample is irradiated by a monochromatic beam with a power $h\upsilon$, the electrons at different energy levels (core energy level and valence band) inside the sample absorb the photon energy. Then the electrons can overcome the work function of the material and escape from the sample. With detection of the energy, angle, and quantity of these emitted photoelectrons, we can obtain information on the electronic structure inside the material. The photoelectrons emitted from the sample move around the sample with a $2\pi$ stereoscopic angle. The electronic structure of the material can be determined according to the measured energy and the number of photoelectrons along different emission directions (Hertz, 1887; Einstein, 1905). This technology can be classified according to the measured physical parameter (energy, momentum, and spin) as shown in Table 2.

According to the measured physical parameters, the PES can be classed as angle-integrated photoelectron spectroscopy (only measurement of energy), angle-resolved photoelectron spectroscopy (measurement of energy and momentum), spin-resolved photoelectron spectroscopy (measurement of energy and spin), and spin- and angle-resolved photoemission spectroscopy (measurement of energy, momentum, and spin).

**Table 2 Photoelectron spectroscopy classified by the measured physical parameter**

| Photoelectron spectroscopy | Parameter(s) | |
|---|---|---|
| | Angle-integrated | Angle-resolved |
| Non-spin-resolved | $E$ | $E$, $k$ |
| Spin-resolved | $E$, $s$ | $E$, $s$, $k$ |

The three parameters of the electrons in the solid, namely, $E$, $k$, and $s$, can describe its electronic structures. These primarily determine the physical properties of the material. By ARPES, the information of energy and momentum can be obtained simultaneously by measuring the number and energy of the photoelectrons along different emission directions of the space. ARPES is a direct tool to measure the electronic structure of materials, many-body effects, and electron dynamics in the study of complex quantum materials. The spin-resolved ARPES can further detect the spin states of materials.

According to Einstein's quantum theory of the photoelectric effect, the experimental schematic of the ARPES working principle is shown in Fig. 27 (Mai, 2013).

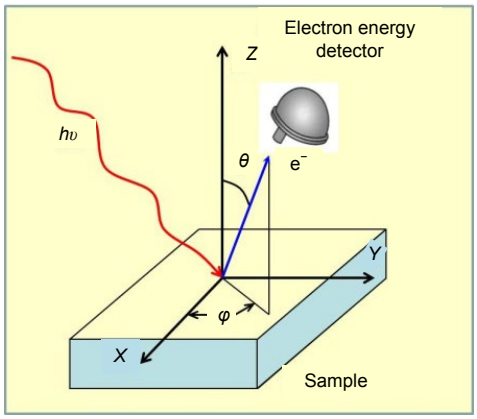


**Fig. 27 Schematic of the experimental geometry of the ARPES working principle (reprinted from Mai (2013), Copyright 2013, with permission from the Science Press)**

An electron energy detector is used to collect these photoelectrons at different angles in space. After measuring the distribution of these photoelectrons with kinetic energy $E_{\mathrm{kin}}$, the photoelectron momentum $p$ is given by

$$p=\sqrt{2mE_{\mathrm{kin}}}, \tag{1}$$

where $m$ is the effective mass of photoelectrons.

Among them, the components of momentum $P$ parallel and perpendicular to the surface of the sample are determined by the polar angle $\theta$ and the azimuth angle $\varphi$. In the process of photoelectron emission, the total energy and the component of the momentum parallel to the surface of the sample are conserved, while the component of the momentum vertical to the surface of the sample is not conserved because of the destruction of surface translational symmetry.

The momentum of the photons can be neglected considering that the energy of photons used in the ARPES experiment is low. Thus, the energy and momentum of the photoelectrons can be linked to the binding energy $E_B$ in the solids and crystal momentum by the following conservation relationships:

$$E_{kin} = h\upsilon - |E_B| - \Phi, \tag{2}$$

$$p_{\parallel} = \hbar k_{\parallel} = \sqrt{2mE_{kin}} \cdot \sin\theta. \tag{3}$$

Here, $\hbar k_{||}$ is the component parallel to the surface of the electron crystal momentum in the extended Brillouin region, and $\Phi$ is the work function. For the much larger $\theta$, the electron momentum detected may reach the high-order Brillouin region. By deducting the inverse lattice vector $G$, the simple electron crystal momentum in the first Brillouin zone can be obtained.

Because of the broken crystal translation periodicity in the direction perpendicular to the surface of the sample, the component of photoelectron momentum perpendicular to the sample $\hbar k_{\perp}$ is no longer conserved, which causes $k_{\perp}$ to be more complicated.

There are several ways to obtain $k_{\perp}$. A convenient and accurate method is to assume the final state of the free electron. In this case, the following formula is obtained:

$$\hbar(k+G) = \sqrt{2m(E_{kin} + V_0)}, \tag{4}$$

where $V_0$ represents the so-called inner potential, which can be obtained by matching the measured energy band with the theoretical calculation result, theoretical approximation, or using the inherent symmetry in the measured energy band.

In a low-dimensional material, the measurement results of ARPES become direct and easy to analyze and explain. For example, in a low-dimensional system with an anisotropic electronic structure, the dispersion that we cannot determine can be basically ignored along the $z$ direction (perpendicular to the surface of the sample, as shown in Fig. 27). $h\upsilon$ is the incident photon energy, $e^-$ represents the emission photoelectrons, and the direction of the emission photoelectrons is determined by $\theta$ and $\varphi$. For example, the electronic structure of copper oxide high temperature superconductors exhibits significant anisotropy and its electronic structure shows mainly quasi-2D.

Note that the light source used in an ARPES experiment usually is in the ultraviolet range ($h\upsilon$< 100 eV), so the high energy and momentum resolutions are easily obtained. As indicated by Eq. (3), momentum resolution $\Delta k_{||}$ is directly correlated with photon energy ignoring the influence of the limited energy resolution:

$$\Delta k_{\parallel} \approx \sqrt{\frac{2mE_{kin}}{\hbar^2}} \cdot \cos\theta \cdot \Delta\theta. \tag{5}$$

$\Delta\theta$ corresponds to the angular resolution of the electron energy analyzer. From Eq. (5), it is evident that low photon energy and large polar angle $\theta$ (measurements can be moved out of the first Brillouin zone) are conducive to enhancing the momentum resolution.

The experimental principle diagram of a modern ARPES is shown in Fig. 28 (Zhou et al., 2018). The hemispherical electron energy analyzer is equipped with a two-dimensional (2D) spatial resolution detector and a multi-element electrostatic input lens. The energy and momentum resolutions of modern electron energy analyzers are significantly improved. The typical energy resolution and angular resolution are better than 1 meV and 0.1°, respectively.

There is a great need to further improve the performance of ARPES in terms of energy and momentum resolution, data acquisition efficiency, system stability, and so on. The ARPES is pushed forward to probe fine electronic structure with extreme conditions by ever richer and deeper physics knowledge of condensed matter physics, which is still a great challenge for ARPES. Now with the latest improvement, ARPES is not only a conventional band mapping tool but also a cutting-edge probe of many-body effects in quantum materials. However, further improvements are urgently needed. Since the light source plays a key role in developing ARPES

performance, great efforts have been made to develop better light sources such as synchrotron radiation light and monochromatic light from gas-discharge lamps. The latest developed DUV-DPL is a new and powerful light source for ARPES experiments with superior and unique advantages. The photoemission technique has been developed to a new level with the DUV-DPL. It leads to great high-quality and significant research studying the fine electron structure of complex quantum materials, such as unconventional superconductors and topological materials (Beamson et al., 1990; Mårtensson et al., 1994; Kiss et al., 2005, 2008).

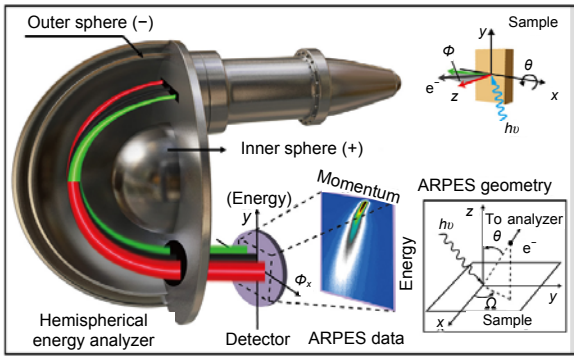


**Fig. 28 Principle of a modern ARPES with a hemispherical electron energy analyzer (reprinted from Zhou et al. (2018), Copyright 2018, with permission from the IOP Publishing Ltd.)**

### 3.1.2 Development of ARPES

The most powerful function of ARPES is that it can directly measure a great number of fundamental physical parameters which directly determine the macroscopic physical properties of a material. The velocity and effective mass of the electron can be obtained from the relationship of the energy-momentum dispersion. The scattering rate can be obtained from the linewidth of the energy distribution curve (EDC) by studying the line type of the spectral spectrum. The size of the superconductor gap or pseudogap can be obtained from the EDC peak or band edge position; by studying the Fermi surface the carrier concentration can be obtained from the bulk of the Fermi surface, and the nesting vector can be obtained from the topological structure of the Fermi surface.

ARPES has been developed to be an important experimental method for the measurement of the energy band structure and Fermi surface of the sample. The performance has been improved significantly in past decades. On one hand, the appearance of some important materials and physical problems has put forward higher and higher demands on performance. On the other hand, the wider application of light sources greatly improves their quality. In particular, resolution and detection efficiency are greatly improved with the appearance and continuous progress of new electron energy analyzers. The progress of ARPES technology is also manifested in the remarkable improvement of angular resolution and the accomplishment of multi-channel measurement of the angle. The modern electron energy analyzer can realize multi-angle-at-a-time measurement, which has dramatically improved the data acquisition efficiency. At present, the optimum resolution can be obtained with the 0.1° best angular resolution.

There are usually two typical kinds of light source: X ray and DUV. With X ray the deep core level electron can be stimulated because of its higher photon energy range, and we can see the abundant information peaks in the spectrum. In 1954 a Swedish scientist Prof. Kai Siegbahn and his team developed the first double-focus magnetic field photoelectron spectrometer in the process of studying the $\beta$ electron energy spectrum (Mai, 2013). This approach is called X-ray photoelectron spectroscopy, XPS for short, because the soft X properties of aluminum and magnesium are mainly used. The most impressive success of XPS technology is the discovery of the chemical shift effect where the spectral peak position of the inner electron changes with the chemical environment of the corresponding atom.

In 1962, Turner et al. first used the helium Ia resonance line (21.22 eV) of inert gas as an ionization source and created a PES with the He I resonance line as the light source (Mai, 2013). This kind of photoelectron spectroscopy is more suitable for studying the electronic state of the valence band, and this complements XPS. This method is called ultraviolet photoelectron spectroscopy, UPS for short, and is in general used to analyze the surface state and shallow level structure.

The gas discharge of UPS is a common light source in experiments. In most cases, helium is the gas used. Its shortcoming is that the photon energy is discontinuous, photon flux is insufficient, the beam

diameter is large, and in general its polarization cannot be tuned.

In 1972, Eastman first used a synchrotron radiation source in a PES experiment and showed the advantage of a continuously adjustable wavelength for the first time. By selecting the appropriate photon energy, the intensity of the photoemission signal in the surface atomic layer can be enhanced, and the information from the extreme surface can be obtained.

### 3.2 Experimental setup of ARPES

The deep ultraviolet laser ARPES mainly consists of four parts: a deep ultraviolet laser, an ultrahigh vacuum system, an electron energy analyzer, and a temperature-controlled sample rotated system.

#### 3.2.1 Deep or vacuum ultraviolet laser by second harmonic generation

Like the gas discharge and synchrotron radiation mentioned above, DUV-DPL has prompted the development of ARPES. The main emphasis of this part is on the progress of a series of ARPESs we have developed based on deep or vacuum ultraviolet laser by second harmonic generation. Table 3 shows the comparison of different typical DUV light sources, which shows the advantages of DUV-DPL compatible to ARPES. From Table 3, we can see that the energy resolution of DUV-DPL ARPES is increased by about one order of magnitude, photon flux by about five orders, and the photon flux density by about seven orders with a rich work mode of ns, ps, and fs and bulk effect of about 10 nm detection depth. ARPES is suitable for observing new phenomena and obtaining new data at the frontier of research in physics and material science (Lanzara et al., 2001; Koralek et al., 2006, 2007; Liu et al., 2008).

Historically, it has been a long time for the laser to be used first as a light source. It is difficult for these early laser-based ARPESs to provide information about the intrinsic electronic properties of the sample because of many disadvantages, such as low linewidth, low pulse repetition rate, low photon flux, and obsolete electron energy analyzers.

To be an excellent laser source for a high resolution ARPES, several basic requirements are summarized as follows (Haight et al., 1988; Haight and Peale, 1994; Karlsson et al., 1996; Nessler et al., 1998; Passlack et al., 2006; Perfetti et al., 2006; Mathias et al., 2007; Graf et al., 2010; Petersen et al., 2011; Rohwer et al., 2011; Zhou et al., 2018):

**Table 3 Comparison of typical DUV light sources**

| Parameter | Value | | |
|---|---|---|---|
| | DUV-DPL | Synchrotron radiation | Gas-discharge light |
| Energy resolution (meV) | About 0.26 | 1–5 | About 1.2 |
| Photon flux (photon/s) | $10^{14}$–$10^{15}$ | $10^{10}$–$10^{12}$ | About $10^{12}$ |
| Density of photon flux (photon/(s·cm$^2$)) | $10^{19}$–$10^{20}$ | $10^{12}$–$10^{14}$ | $<10^{14}$ |
| Wavelength range (nm) | 164.9–232 | 1–210 | 58.5 (He) |
| Operation mode | ns, ps, fs (1 Hz–1 GHz) | ns, ps pulse (5–500 MHz) | Continuous wave |
| Detection depth (nm) | About 10 (bulk effect) | 0.5–2 (surface effect) | About 0.5 (surface effect) |

1. Suitable photon energy: considering all the factors, the 6–15 eV photon energy is a suitable range for a super high resolution ARPES.

2. High photon flux: the laser source should have a high enough photon intensity to obtain quite a good photoemission signal for a high signal-to-noise ratio and high data acquisition efficiency.

3. Narrow linewidth: the linewidth should be as narrow as possible to obtain high energy resolution of ARPES.

4. Continuous-wave (CW) or quasi continuous-wave (QCW) laser source: the CW or QCW (about 100 MHz) laser may minimize the space charge effect. The space charge effect may change the energy position, increase the linewidth, and distort the line shape of the photoemission spectra for high energy resolution and the inherent signal (Passlack et al., 2006; Graf et al., 2010).

5. Long-time stability: during the ARPES working process the measurement process usually continues for several days and the laser must remain stable during the whole process.

6. Polarization adjustable: sometimes, the arbitrarily adjustable polarizations are more important than high power. For arbitrarily adjustable polarization the photoelectric emission matrix element effect can be used and the orbital characteristics of the energy bands are achieved. Moreover, circular polarization is suitable for studying the magnetism or the test time reversal symmetry breaking. Thus, the arbitrary direction linear, circular, or elliptical polarization, left- or right-handed, is necessary without any sacrifice of other measurement parameters.

7. Easily adjustable beam diameter size (<1 mm): a small beam diameter size is ideal to improve the performance of the electron energy analyzer and measure of a small area of a sample. Unfortunately, a small beam diameter size will cause a strong space charge effect. To achieve a good balance between a small beam diameter and a weak space charge effect on different samples, it is necessary that the beam diameter size be adjustable.

8. Matching electronic energy analyzer: the lower the kinetic energy of laser photoelectrons, the stricter the demand on the electron energy analyzer. The electron energy analyzer should work normally with the angular mode and super high energy resolution at a lower electron kinetic energy.

9. Compact and simple structure: this will greatly reduce the requirements of building, operational cost, and laboratory space.

10. Convenient operation: operation of the laser should be easy to learn and convenient for non-professionals.

11. Other requirements: pulse duration, the pulse repetition rate, and convenient wavelength tunability are equally important, especially for the time-resolved ARPES.

The three kinds of light sources are complementary to the ARPES experiments considering the advantages and disadvantages mentioned above.

The helium lamp is still widely used in most ARPES labs. Because of compact structure and CW emission, the gas discharge lamp has no space charge effect. It has some obvious drawbacks: insufficient photon flux, fixed photon energy, fixed polarization, large beam diameter size, difficulty in focusing, and easy leak of helium gas to the measurement chamber.

In the past decades, the continuous progress of synchrotron technology and the technical advancement of the 2D detector type hemispherical electronic energy analyzers greatly improved the performance of ARPES. This makes it an advanced technology for detecting electronic structure and multi-body interaction in condensed matter. It can facilitate the measurement of small or inhomogeneous samples. It is still very difficult for synchrotron based ARPES to obtain a super high energy resolution better than 1 meV because the narrow linewidth is obtained at the great sacrifice of reduction of photon flux. The photon flux usually is too low to be enough for ARPES measurement when the linewidth reaches the 1 meV level.

The newly developed DUV-DPL ARPES has many distinctive advantages, such as high resolution (energy, momentum, and spin resolution), low space charge effect, high efficiency, compactness, and low cost. The data acquisition efficiency and data quality can be greatly improved based on an extremely high and stable photon flux. It is convenient to obtain super high energy resolution during ARPES measurement with narrow linewidth of DUV-DPL. The most important aspect is that the linewidth and photon flux are uncorrelated and can be optimized independently, which is, in particular, superior to a synchrotron radiation source. The use of DUV-DPL has broken the bulwark of super high energy resolution 1 meV, which has always hindered the development of ARPES technology and is a dream that the scientists have been pursuing for decades. At the same time, we can obtain high momentum resolution and enhance bulk sensitivity with a relatively low photon energy. It is very easy to control the polarization of DUV-DPL and adjust the beam diameter size (Zhou et al., 2018).

The combination of excellent DUV-DPL and other new technologies of ARPES makes the ARPES updated, and the new generation ARPES has exhibited its superior performance.

#### 3.2.2 Electron energy analyzer

1. Hemispherical electron energy analyzer

The electron energy analyzer is one of the core parts of ARPES. Almost all modern ARPESs use the hemispherical electrostatic energy analyzer, which is composed of two concentric hemispheres with a high precision electrostatic voltage in each hemisphere. At present, the typical hemispherical electron energy analyzer is equipped with high energy and momentum resolutions, multi-channel-angle-detection measure-

ment ability, and has high transmission performance. The energy and momentum resolutions are better than 1 meV and ±0.1°, respectively.

The two most outstanding features of the new electron energy analyzer are the super high energy resolution and the simultaneous 2D detection of electron energy and angle. Taking the widely used electron energy analyzer as an example, the whole apparatus consists of four parts according to the order of electronic transmission: multiple electrostatic lenses, electrostatic hemispherical analyzer, slit structure, and electronic detection system.

2. Time-of-flight electron energy analyzer

The recently developed time-of-flight electron energy analyzer is a promising new type of electron energy analyzer for ARPES. This energy analyzer determines the kinetic energy by measuring the time of flight of photoelectrons from the sample surface to the detector. The most significant advantage is that it is developed from the awkward fact that only a line (one-dimensional momentum) of the momentum space was measured in the past, but now there is the convenience that a plane (2D momentum) is measured simultaneously. Therefore, the measurement efficiency can be increased by a factor of hundreds. Because of the limitation of the flight time of electron from the sample surface to the detector, this type of analyzer is currently suitable for light sources with relatively low pulse repetition rates (from hundreds of hertz to several megahertz) and particularly for high resolution ARPES with laser.

This kind of analyzer is actually the combination of multi-electron lens technology for hemispherical electron energy analyzers and a traditional product of the time-of-flight ion energy analyzer for time-of-flight mass spectrometers. The angle of one-time detection is about 250 times higher than that of the hemispherical electron energy analyzer. The energy resolution of the new time-of-flight electron energy analyzer can reach 0.15 meV, the angular resolution can reach 0.08°, and the angle range detected at the same time can reach ±15°.

#### 3.2.3 Ultra-high vacuum system

The ARPES technique is very sensitive to the sample surface, so it is critical to have a clean sample surface, that is, an excellent crystal surface. The valence electrons of the impurities in the crystal surface contribute to the photoelectron spectrum. If these impurities form any chemical bond with the crystal, the valence electron spectrum of the crystal will be affected.

Typical ARPES experiments are performed in ultra-high vacuum on a clean and flat sample surface. To obtain the ultra-high vacuum (usually better than $5\times10^{-9}$ Pa), baking and filament degassing are required. Each vacuum chamber is equipped with the necessary vacuum measurement, residual gas analysis, and other instruments. To transfer samples quickly without damaging the ultra-high vacuum in the analysis chamber and avoid baking the sample, a multi-stage sample grading transfer system is used.

#### 3.2.4 Temperature-controlled sample rotated system

On one hand, the sample is required to rotate freely to measure the momentum in any direction; on the other hand, the sample must be able to reach a low temperature, so that temperature-induced spectrum linewidth broadening can be avoided. However, the two requirements are often incompatible because the increase of the sample rotating ability will increase the complexity of the rotating mechanical structure and make it difficult for the sample to reach the low temperature.

Manipulation of the sample is accomplished by a sample controller with three translational degrees of freedom ($X$, $Y$, $Z$) and a low cryogenic goniometer with three rotating degrees of freedom, which can realize the translation and rotation of the sample in the whole space.

All the translation and rotation can be accurately realized by a computer-controlled stepper motor compatible with vacuum. A typical cryogenic sample angle instrument is cooled by continuously flowing liquid nitrogen.

### 3.3 ARPES prototypes based on DUV-DPL

DUV PES systems at the Institute for Solid State Physics of the University of Tokyo are also cited in this part. Some experimental applications of these two kinds of PESs are also introduced, including the detection of fine electronic structures and low-$T_c$ superconductors.

The first generation PES system at the Institute for Solid State Physics was used in 2005, and the energy resolution was as fine as 360 μeV with $T$ as

low as 2.9 K. The second generation operated since 2012 has 70 μeV energy resolution and 1.5 K.

The fundamental 355 nm laser has a 80 MHz pulse repetition rate, which is generated from a frequency-tripled Nd:$YVO_4$ laser. The linewidth of the 177 nm laser is 260 μeV with an about 10 ps pulse duration. The average output power is 2.5 mW with a photon flux of $2.2\times10^{15}$ photons/s. The linear ($p$ or $s$) or circular polarizations, left- or right-handed, can be obtained easily with a $\lambda/2$ wave plate and a $\lambda/4$ wave plate. An electron analyzer was also developed, and its best performance was theoretically estimated to be 250 μeV.

The second generation was developed to further improve the total energy resolution and cooling ability. A vertical-type cryostat was developed and the thermal shields surrounding the samples were improved to reduce further thermal radiation. The linewidth of 177.3 nm was 25 μeV with an etalon to reduce the linewidth of the fundamental laser. A new type of hemispherical electron analyzer was used.

As far as the main applications of the DUV angle integrated PES were concerned, the quasiparticle properties in the superconducting state and the observation of anomalous electronic structure near the Fermi level were investigated. Compared with the PES using other photon sources, low-$T_c$ and high energy resolution DUV AIPES showed a marked improvement in the sharpness of the spectra. The unusual gap and/or peak evolutions near $E_F$ have been detected based on its high energy resolution of DUV AIPES. The bulk sensitivity and high photon flux of the DUV laser are also suitable for the investigation of chemically unstable materials and systems with low carrier density. For example, the two-gap superconductivity in $Mg(B,C)_2$ and the rattling and superconductivity in $KOs_2O_6$ were investigated. The Kondo resonance in 3D transition-metal oxide $LiV_2O_4$, pseudogap in water-intercalated superconductor $Na_xCoO_2{\cdot}yH_2O$, and multiphonon sidebands in B-doped diamond superconductors were experimentally researched with DUV AIPES.

As far as the applications of ARPES based on DUV-DPL were concerned, the band dispersions near the Fermi level and the superconducting mechanism of iron-based superconductors were investigated based on its strong advantages of high energy and momentum resolutions. For example, the investigations of the low energy kinks for the high-$T_c$ cuprate $(Bi, Pb)_2(Sr, La)_2CuO_{6+\delta}$ and topological insulator $Bi_2Se_3$ families were introduced. The ground state of the parent compound $BaFe_2As_2$, superconducting gap symmetry in optimally doped $BaFe_2(As,P)_2$, doping-dependent superconducting gaps in $BaKFe_2As_2$, superconducting gap nodes in $KFe_2As_2$, and composite BCS-BEC superconductivity in Fe(Te,Se) were experimentally researched.

In this article, we will introduce mainly the research on a series of ARPES prototypes based on DUV-DPL that our scientific research team has developed, which have many advantages over traditional light sources: (1) a super high energy and momentum resolution ARPES prototype based on DUV-DPL with 177.3 nm fixed wavelength and 175–210 nm widely tunable wavelength; (2) spin- and angle-resolved PES (SARPES) prototype based on arbitrarily adjustable polarization DUV-DPL; (3) angle-resolved time-of-flight PES (ToF ARPES) prototype based on adjustable pulse repetition rate DUV-DPL.

#### 3.3.1 Super high energy and momentum resolution ARPES prototype based on DUV-DPL with 177.3 nm fixed wavelength and 175–210 nm widely tunable wavelength

The advantages of this kind of super high energy and momentum resolution ARPES prototype are the two types of DUV-DPL and the advent of a new electron energy analyzer. The DUV-DPL with 177.3 nm fixed wavelength and 175–210 nm widely tunable wavelength has ps level pulse duration and MHz level pulse repetition rate. The angular mode of the new electron energy analyzer can work properly at a DUV electron kinetic energy. The ARPES based on DUV-DPL has exhibited superior performance with super high energy resolution less than 1 meV, super high photon flux density, high momentum resolution, highly enhanced bulk sensitivity, and so on.

Fig. 29 shows the entity photo of super high energy and momentum resolution ARPES prototype based on DUV-DPL with 177.3 nm fixed wavelength and 175–210 nm widely tunable wavelength.

The two DUV laser beams are focused on the sample in the analysis chamber by a $CaF_2$ lens. The analysis chamber is isolated from the optical chamber of DUV-DPLs in vacuum by a $CaF_2$ window.

The energy resolution of the 177.3 nm DUV-DPL is about 0.26 meV, which is very much narrower than the other light sources. With the resolution of the advanced electron energy analyzer, we have obtained an overall instrumental high energy resolution of 0.36 meV and a momentum resolution of 0.071 $nm^{-1}$. The maximum in-plane momentum covered is 8.4 $nm^{-1}$ with a work function of 4.3 eV and photon energy of 177.3 nm.

The 177.3 nm may nearly reach the important ($\pi$, 0) region of many important and novel materials, such as high-$T_c$ cuprate superconductors, the iron-based superconductors, and many other transition metal oxides (Jiang et al., 2014; Huang et al., 2016; Wu et al., 2016; Zhang Y et al., 2017).

From the experimental results, the 177.3 nm DUV-DPL has a disadvantage of its single photon energy. Because of the photoemission matrix element effects, the measurements with a single 177.3 nm photon energy may miss some energy bands or, in the worst case, may not operate on some materials. Widely tunable wavelengths with different photon energies are necessary to obtain electronic structure at different $k_zS$, especially for some materials with significant $k_z$ dispersion. It should be equipped with widely tunable wavelength.

The DUV-DPL with tunable wavelength offers a great chance to provide a 175–210 nm widely tunable wavelength for ARPES. The photon energy may change from 5.9 to 7.1 eV (175–210 nm) and from 3.0 to 3.5 eV (355–420 nm). The pulse duration is about 1.5 ps at 200 nm with an 80 MHz pulse repetition rate. With the two "twins" BBO crystals placed head to head, we obtain the 350–420 nm wavelength with one knob conveniently with high output power and unchanged beam propagation direction during wavelength tuning. The 175–210 nm wavelength is also focused on the sample in the analysis chamber with a $CaF_2$ lens. We have developed a ps 175–210 nm widely tunable wavelength DUV-DPL prototype and applied it to the ARPES prototype (Fig. 29).

### 3.3.2 Spin- and angle-resolved PES prototype based on arbitrarily adjustable polarization DUV-DPL

The spin state of materials has played an increasingly important role because of the rapid progress in both fundamental studies and potential applications, especially for the topological quantum state and spintronics. Therefore, a number of scientists have been devoted to the development of SARPES, which is the combination of ARPES technology with spin detector technology. We have developed a SARPES prototype based on an arbitrarily adjustable polarization DUV-DPL, and the entity photo of the prototype is as shown in Fig. 30, which has two major parts: the arbitrarily adjustable polarization DUV-DPL and the SARPES system.

**Fig. 29 Entity photo of super high energy and momentum resolution ARPES prototype based on DUV-DPL with 177.3 nm fixed wavelength and DUV-DPL with 175–210 nm widely tunable wavelength**

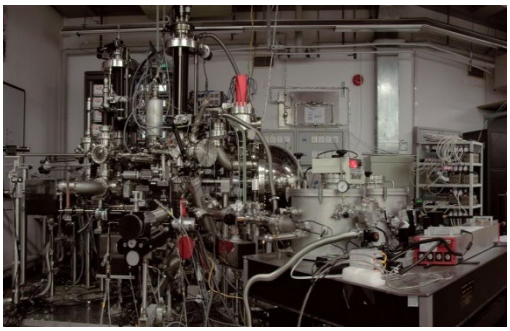

**Fig. 30 Entity photo of the SARPES prototype based on arbitrarily adjustable polarization DUV-DPL**

The linewidth of synchrotron-based SARPES will reduce to a poor energy resolution 50–100 meV to increase the photon flux. Many kinds of spin detectors have been developed for SARPES and each one has its own advantages and disadvantages.

There is a good chance to increase the performance of SARPES based on arbitrarily adjustable polarization DUV-DPL, which can easily compensate for the low efficiency of other light sources and provide arbitrarily tunable polarization to the Mott spin detector without losing the overall high energy resolution. Fig. 31 is shown as the structure diagram of

SARPES based on arbitrarily adjustable polarization DUV-DPL (Zhou et al., 2018).

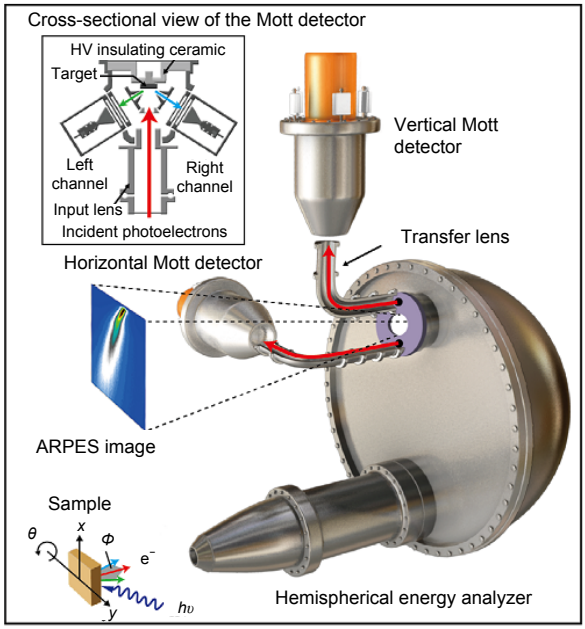


**Fig. 31 Working principle of a SARPES equipped with two Mott type spin detectors, where the inset is the cross-sectional view of the Mott detector (reprinted from Zhou et al. (2018), Copyright 2018, with permission from the IOP Publishing Ltd.)**

The best spin-resolved energy resolution of about 2.5 meV is obtained benefiting from the intrinsic narrow linewidth (about 0.26 meV) and super high photon flux. The result is comparable to the best result 1.7 meV achieved so far for the SARPES measurement (Xie et al., 2014). The best angular resolution is about 0.3° and the corresponding momentum resolution can be further improved.

The other excellent merits of this kind of SARPES are as follows:

1. The three variables of energy, momentum, and spin can be obtained at the same time.

2. The three spin components of photoelectrons can be probed simultaneously.

3. The arbitrary direction linear, circular, or elliptical 177.3 nm polarizations, left- or right-handed, can be tuned conveniently.

4. The new analyzer can cover 2D momentum space conveniently without rotating the sample. This not only ensures no unnecessary mechanical rotation of sample, but also maintains the same polarization geometry during the measurements.

We demonstrated the spin- and angle-resolved capability measured simultaneously on Au(111) surface states. These experimental results are identical to the previous results and verify the spin-resolving capability.

3.3.3 Angle-resolved time-of-flight PES (ToF ARPES) prototype based on adjustable pulse repetition rate DUV-DPL

Electrons are emitted in the entire 2π solid angle during the photoemission process. The latest generation of the angle-resolved time-of-flight electron energy analyzer is developed just for covering the 2D angle space simultaneously. This overcomes the shortcomings of the first two generations of the electron energy analyzer. This is a huge leap because the data acquisition efficiency increases significantly. The entity photo of ToF ARPES based on pulse repetition rate adjustable DUV-DPL is shown in Fig. 32.

**Fig. 32 Entity photo of ToF ARPES based on pulse repetition rate adjustable DUV-DPL**

A ps 177.3 nm DUV-DPL with an adjustable pulse repetition rate from a low pulse repetition rate 0.2 MHz to a high one 1 MHz is used. It has distinct advantages as follows:

1. Two-dimensional momentum spaces are measured simultaneously and the efficiency of momentum coverage is improved by more than two orders of magnitude. It is a basic change of the ARPES technique. It had been impossible before to observe the Fermi surface in real time, while it becomes a reality now. It had been hard to resolve the problem of revealing fine electronic structure, but now it becomes helpful because the two dimension angles can be measured under the same condition.

2. Energy and momentum resolutions are high.

3. The number of electrons hitting the detector is

counted directly by the time-of-flight analyzer. During the measurement process there is low background and the signal nonlinearity effect that is usual in an analyzer is suppressed.

To verify the performance, an experiment was carried out to measure the Fermi edge of a polycrystalline Au sample. The 177.3 nm DUV-DPL has an adjustable pulse repetition rate, and the sample temperature is about 9.5 K (a Fermi edge width of 3.37 meV) (Reber et al., 2014). The results are shown in Fig. 33 (Zhou et al., 2018). The space charge effect of the same polycrystalline Au was measured with different powers and repetition rates of laser. Based on the experimental results the overall instrumental energy resolution is better than 1 meV after subtracting the temperature broadening. The space charge effect was obvious when the beam diameter was 0.1 mm and the pulse repetition rate was 200 kHz, and it nearly disappeared if the pulse repetition rate was near 1 MHz.

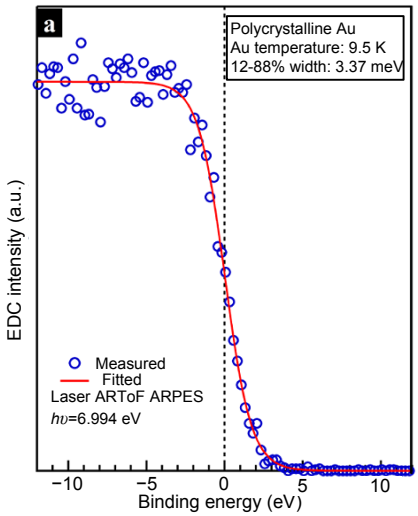


**Fig. 33 Experimental results of polycrystalline Au with ToF ARPES (reprinted from Zhou et al. (2018), Copyright 2018, with permission from the IOP Publishing Ltd.)**

From the experimental measurements on an optimally doped $Bi_2Sr_2CaCu_2O_{8+\delta}$ (Bi2212) superconductor measured at 15 K, high-quality band structure along any momentum cut can be extracted. The experimental data was continuous in the covered momentum space, and thus difficult to obtain in the past with the routine ARPES technology. We also measured the nonlinearity effect at a low count rate and a high count rate along the same momentum cut following a proposed procedure. The experimental data showed that there is approximately no nonlinearity effect. The result is further demonstrated by the same line shape of two photoemission spectra measured using different count rates.

## 4 Frontier scientific research

In this part, we focus mainly on research front applications in unconventional superconductors and topological materials with ARPES prototypes based on DUV-DPL.

### 4.1 New coupling mode and extraction of Eliashberg functions

ARPES based on DUV-DPL is a powerful instrument to investigate many-body effects in materials with the latest improvement technique, including superior energy and momentum resolution and high data statistics. It is especially important to understand the anomalous normal state properties and the superconductivity mechanism of the high temperature cuprate superconductors. An experiment on studying nodal band renormalization in a Bi2212 superconductor was done specifically to show the power of this kind of ARPES. New scientific features such as a dip-like feature at about 115 meV and a hump structure at about 150 meV at high energies emerge. These had not been resolved before. They are present only in the superconducting state and their amplitude gets stronger when the temperature decreases. The energy scale of phonons in Bi2212 is below 100 meV, so these new energy scales are unlikely caused by electron coupling with phonons. Perhaps there are some new mode couplings in the superconducting state of Bi2212 (Bogdanov et al., 2000; Johnson et al., 2001; Kaminski et al., 2001; Zhou et al., 2003; Shi et al., 2004; Zhang HJ et al., 2008).

It is difficult to understand the superconductivity mechanism when studying high-temperature superconductors and how the electrons interact and form Cooper pairs. The BCS superconductivity theory of conventional superconductors is not suitable for high temperature cuprate superconductors because high $T_c$ superconductors show a *d*-wave superconducting order parameter that is different from the *s*-wave case in conventional superconductors like Pb. Under these

circumstances, experimental tools that have momentum resolution are necessary. This idea has been shelved for more than 15 years without any attempt or progress because of the lack of ARPES with extremely high precision for such analyses.

The new progress of DUV-DPL ARPES makes it possible to solve the key problem of the pairing mechanism in high temperature cuprate superconductors by extracting the pairing Eliashberg functions in the superconducting state. It is necessary to obtain high data precision (better than 1%) for measurement of such a weak superconductivity-induced effect because the pairing self-energy and then the pairing Eliashberg function are obtained from the signal difference between the superconducting state and the normal state. High energy and momentum resolutions are necessary. This is the first time that the normal Eliashberg function and the pairing Eliashberg function have been extracted from the experimental data, and the critical information on examining various theoretical models to understand high-temperature superconductivity can be obtained.

### 4.2 Direct observation of spin-orbital locking in topological insulators

Due to the unique electronic structure, spin texture, and the novel physical properties, topological insulators have attracted a lot of attention. The electron spin and its crystal momentum are locked together in its metallic surface state with helical spin texture. The spin texture might be coupled with the orbital texture in topological insulators, which is also predicted by theory. If such a new spin-orbital texture can be proved by experiment, the significance is that it can promote new and direct thinking on the spin texture of topological insulators. High resolution spin-resolved ARPES is a necessary choice to directly prove the possible spin-orbital locking in topological insulators (Zhang WT et al., 2008).

All the demands of spin-orbital locking in topological insulators can be satisfied by SARPES based on DUV-DPL. Arbitrary direction linear polarization states of the DUV-DPL with *s*- or *p*-polarization geometry were easily tunable for orbital-selective SARPES measurements. The photoemission matrix element effects gave a huge advantage when different orbital textures of the $Bi_2Se_3$ Dirac surface state were observed. The spin texture of the $Bi_2Se_3$ topological surface state with different polarization geometries was further measured. The spin texture was confirmed. The relationship between the spin and orbital textures was revealed with systematic experimental data of the momentum-dependent spin polarization of the Dirac cone in *s*- and *p*-polarization geometries. The usual spin picture in topological insulators cannot describe the data obtained. However, they were fully consistent with the predictions on spin-orbital locking. The data thus provided strong experimental evidence for the orbit-selective spin texture in the $Bi_2Se_3$ topological insulator (Bok et al., 2010; Zhang HJ et al., 2013).

### 4.3 Novel electronic structure of $WTe_2$ and $ZrTe_5$

#### 4.3.1 Complete electronic structure and topological nature of $WTe_2$

$WTe_2$, with extremely large magnetoresistance, has attracted great attention because of the compensation of electrons and holes in the material. The prerequisite premise of complete understanding of its electronic structure is to confirm the origin of the anomalous transport properties. There is still a lot of dispute about the full electronic structure of $WTe_2$ because of the existence of multiple pockets in a limited momentum space. It is theoretically forecast that $WTe_2$ is the first candidate that may realize a type-II Weyl state, and this causes great debate. However, there is no sufficient experimental evidence of type II Weyl Fermions in $WTe_2$ (Ali et al., 2014; Soluyanov et al., 2015).

An entire description of the electronic structure of $WTe_2$ has been obtained with superior instrumental resolution. The experimental results show the Fermi surface of $WTe_2$ where the existence of a surface state is clearly identified. The experimental data and results provide electronic evidence that is consistent with the type-II Weyl state in $WTe_2$, although much research is required to fully confirm the realization of type-II Weyl state in $WTe_2$. It is possible to resolve accurately the electron and hole concentrations and their temperature dependence with the first entire $WTe_2$ electronic structure including near-$E_F$ energy bands and all the Fermi pockets.

The experimental results also provide evidence that the temperature range of electron-hole compensation, if exists, is very narrow and there is an electron-hole imbalance over most of the temperature

range. These phenomena are not consistent with the perfect electron-hole compensation picture that is commonly considered to be the cause of the unusual magnetoresistance in $WTe_2$ and provide a new approach for understanding the origin of unusual magnetoresistance in $WTe_2$ (Smith and Traum, 1973; Zhang WT et al., 2013; Smallwood et al., 2014; Shimojima et al., 2015; Wang CL et al., 2017).

4.3.2 Temperature-induced Lifshitz transition and topological nature in $ZrTe_5$

Topological materials have been well researched recently because of their peculiar physical properties, spin texture, and unique electronic structure.

$ZrTe_5$ has been puzzling for a long time because of its anomalous transport properties that are manifested by its unusual resistivity peak and a sign reversal of the Hall coefficient and thermopower. Its origin, however, is still elusory. Recently, it has attracted attention because single layer $ZrTe_5$ may be a 2D topological insulator and there may be a topological phase transition in bulk $ZrTe_5$. However, the topological nature of $ZrTe_5$ remains under debate.

With the great advantage of high resolution ToF ARPES based on DUV-DPL, the electronic structure and its detailed temperature evolution of $ZrTe_5$ are revealed. The experimental data showed the direct electronic evidence of the temperature-induced Lifshitz transition in $ZrTe_5$ and helped determine the underlying origin of transport anomaly at about 135 K. One-dimension-like electronic characteristics observed during the experiment from the edges of the cracked $ZrTe_5$ samples indicated that $ZrTe_5$ is a weak topological insulator (Sobota et al., 2013; Wang YH et al., 2013; Won, 2014).

## 5 Expectation and development

ARPES has become a useful tool for designing novel quantum materials in the condensed matter field. The research on many outstanding physical problems is also always calling for further function improvement. A new way for endowing ARPES with its unique functions is the appearance of DUV-DPL. Tremendous strengths in the research on quantum materials like high temperature superconductors and topological materials have been exhibited through experiments. With the rapid development of technology and increasing experimental demands, ARPES should seek further function upgrading. It is true that there is also space for improvement of DUV-DPL ARPES, and continuous progress may be achieved in the following areas.

### 5.1 Further progress of DUV-DPL

It is essential to further increase the unique performance of this key component of ARPES. Many efforts along these directions have been made, pursuing larger photon energy, narrower linewidth, shorter pulse duration, higher photon flux, more widely tunable wavelength range, more precise regulation (such as smaller beam diameter and more precise beam pointing direction of laser), and continuous wavelength.

The continuous wavelength DUV-DPL is the most perfect light source that does not produce space charge effect theoretically (Taniuchi et al., 2015). To detect the intrinsic electronic structure and information about phase separation or multiple domains of spatially inhomogeneous samples or other new ones, where it is hard or impossible to obtain large enough single crystals, the spatially resolved ARPES is necessary and irreplaceable. Therefore, DUV-DPL with continuous wavelength or focus of microns or sub-microns is the next generation laser to be developed.

The more widely tunable wavelength has a larger range of photon energy. This helps deal with the photoemission matrix element effects and increases the variety of measuring materials, especially with the strong 3D electronic structure.

The time-resolved ARPES is a powerful instrument for investigating electron dynamics and non-equilibrium state. The energy is at the meV level and the time is at the fs level when electronic dynamics is going on for strongly correlated systems, such as high temperature superconductors. The ultrashort pulse and high energy resolution DUV-DPL with high pulse repetition rate, narrow linewidth, and tunable probe pulse is helpful for time-resolved ARPES applications.

For example, we have been developing several new kinds of DUV-DPLs with a shorter wavelength of 164.9 nm and a widely tunable wavelength range of 155–170 nm.

An ns 164.9 nm DUV-DPL with a maximum average power of 6.8 mW was obtained by the eighth harmonic generation of a homemade 1319 nm Nd:YAG laser. The experimental scheme is shown in Fig. 34 (Dai et al., 2016).

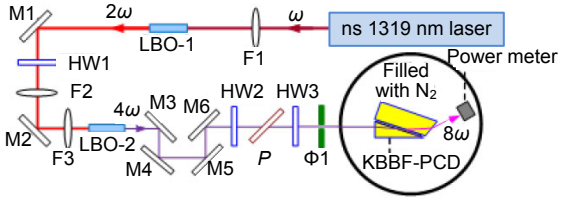


**Fig. 34 Experimental scheme of ns 164.9 nm DUV-DPL (reprinted from Dai et al. (2016), Copyright 2016, with permission from the IOP Publishing Ltd.)**

The relationship between the output power at 164.9 nm and pump power at 329.6 nm is shown in Fig. 35. As far as we know, 164.9 nm is the shortest DUV wavelength generated through the SHG method of solid state laser below 170 nm (Dai et al., 2016). The photo of the 164.9 nm DUV-DPL experimental setup is shown in Fig. 36.

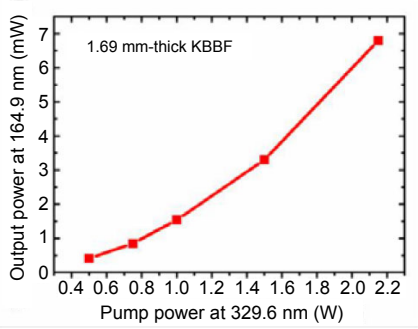


**Fig. 35 Output power at 164.9 nm versus pump power at 329.6 nm (reprinted from Dai et al. (2016), Copyright 2016, with permission from the IOP Publishing Ltd.)**

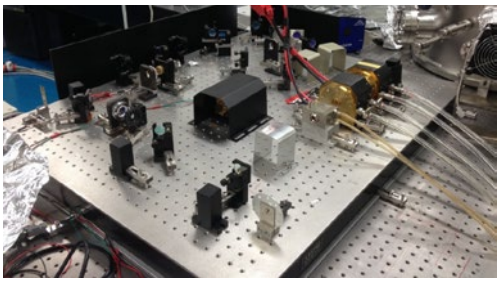

**Fig. 36 Photo of the 164.9 nm DUV-DPL experimental setup**

The results lay an experimental foundation for the development of a ps high pulse repetition rate 164.9 nm DUV-DPL, which is very suitable for ARPES for materials with small lattice constants, larger Brillouin zone, important (π, 0) antinodal region of high $T_c$ superconductors, or other transition metal oxides.

### 5.2 Comprehensive promotion of photoelectron detection technology

The latest third-generation electron energy analyzer can realize a 2D area of angle measurement. The ideal photoelectron detection can cover a full 180° solid angle at the same time. This should be quoted to all the electron energy analyzers. The urgency of μeV level energy resolution needs to be promoted for the development of higher energy resolution photoelectron detection to meet the huge demands of scientific experiments. It is a future development direction to expand concurrent spin state detection during the ARPES measurement of the 2D momentum space. The advanced photoelectron detection techniques are under great development and will be used in all analyzers in the future.

### 5.3 Precise temperature control of the sample

The spectrum will be broadened when the sample temperature rises, so it is imperative to lower the sample temperature to below 1 K. This is necessary for studying materials at low temperatures. We are developing ARPES based on DUV-DPL with extremely high resolution, short wavelength (167 nm), and ultra-low temperature (below 1 K) cryostats.

### 5.4 Integration with multiple advanced technologies

The more complete information of images and data from various aspects we obtain, the more precise an insight into the deep physical mechanism can be. The combination of advanced photoemission technologies and related supporting technologies, for instance, angle-, spin-, space-, and time-resolved photoemission, is an optimal choice. The relative supporting technologies include structural analysis tools to obtain electronic structure and lattice and magnetic structures simultaneously. The compounded ARPES of in situ sample preparation (like molecular beam epitaxy) and in situ sample characterization

(like scanning tunneling microscope) for a clean and flat sample surface is suitable and will become popular in the future.

## 6 Conclusions

In this paper, we have reviewed mainly a series of DUV-DPLs and equipped ARPESs that our research team has developed over more than 20 years. A brief account of typical frontier research results has been given. We believe that DUV-DPL will play a more important role in the field of ARPES. Moreover, ARPES based on DUV-DPL will provide a powerful research platform for the frontier of science.

### Compliance with ethics guidelines

Zu-yan XU, Shen-jin ZHANG, Xing-jiang ZHOU, Feng-feng ZHANG, Feng YANG, Zhi-min WANG, Nan ZONG, Guo-dong LIU, Lin ZHAO, Li YU, Chuang-tian CHEN, Xiao-yang WANG, and Qin-jun PENG declare that they have no conflict of interest.

### References

Ali MN, Xiong J, Flynn S, et al., 2014. Large, non-saturating magnetoresistance in $WTe_2$. *Nature*, 514(7521):205-208. https://doi.org/10.1038/nature13763

Beamson G, Briggs D, Davies SF, et al., 1990. Performance and application of the Scienta ESCA300 spectrometer. *Surf Interf Anal*, 15(9):541-549. https://doi.org/10.1002/sia.740150908

Bogdanov PV, Lanzara A, Kellar SA, et al., 2000. Evidence for an energy scale for quasiparticle dispersion in $Bi_2Sr_2CaCu_2O_8$. *Phys Rev Lett*, 85(12):2581-2584. https://doi.org/10.1103/PhysRevLett.85.2581

Bok JM, Yun JH, Choi HY, et al., 2010. Momentum dependence of the single-particle self-energy and fluctuation spectrum of slightly underdoped $Bi_2Sr_2CaCu_2O_{8+\delta}$ from high-resolution laser angle-resolved photoemission. *Phys Rev B*, 81(17):174516. https://doi.org/10.1103/PhysRevB.81.174516

Chen CT, 2004. Recent advances in deep and vacuum-UV harmonic generation with KBBF crystal. *Opt Mater*, 26(4):425-429. https://doi.org/10.1016/j.optmat.2004.02.007

Chen CT, Xu ZY, Deng DQ, et al., 1996. The vacuum ultraviolet phase-matching characteristics of nonlinear optical $KBe_2BO_3F_2$ crystal. *Appl Phys Lett*, 68(21):2930-2932. https://doi.org/10.1063/1.116358

Chen CT, Xu ZY, Lü JH, et al., 2004. Variable-frequency laser coupler with non-linear optical crystal. Chinese Patent No. CN1172411C (in Chinese).

Chen CT, Kanai T, Wang XY, et al., 2008. High-average-power light source below 200 nm from a $KBe_2BO_3F_2$ prism-coupled device. *Opt Lett*, 33(3):282-284. https://doi.org/10.1364/OL.33.000282

Chen CT, Wang GL, Wang XY, et al., 2009. Deep-UV nonlinear optical crystal $KBe_2BO_3F_2$—discovery, growth, optical properties and applications. *Appl Phys B*, 97(1): 9-25. https://doi.org/10.1007/s00340-009-3554-4

Couprie ME, 2014. New generation of light sources: present and future. *J Electron Spectrosc Relat Phenom*, 196:3-13. https://doi.org/10.1016/j.elspec.2013.12.007

Cyranoski D, 2009. Materials science: China's crystal cache. *Nature*, 457(7232):953-955. https://doi.org/10.1038/457953a

Dagotto E, 2005. Complexity in strongly correlated electronic systems. *Science*, 309(5732):257-262. https://doi.org/10.1126/science.1107559

Dai SB, Zong N, Yang F, et al., 2015. 167.75-nm vacuum-ultraviolet ps laser by eighth-harmonic generation of a 1342-nm Nd:$YVO_4$ amplifier in KBBF. *Opt Lett*, 40(14): 3268-3271. https://doi.org/10.1364/OL.40.003268

Dai SB, Chen M, Zhang SJ, et al., 2016. 2.14 mW deep-ultraviolet laser at 165 nm by eighth-harmonic generation of a 1319 nm Nd:YAG laser in KBBF. *Laser Phys Lett*, 13(3):035401. https://doi.org/10.1088/1612-2011/13/3/035401

Damascelli A, Hussain Z, Shen ZX, 2003. Angle-resolved photoemission studies of the cuprate superconductors. *Rev Mod Phys*, 75(2):473-541. https://doi.org/10.1103/RevModPhys.75.473

Einstein A, 1905. Generation and conversion of light with regard to a heuristic point of view. *Ann Phys*, 322(6):132-148. https://doi.org/10.1002/andp.19053220607

Fujii T, Kumagai H, Midorikawa K, et al., 2000. Development of a high-power deep-ultraviolet continuous-wave coherent light source for laser cooling of silicon atoms. *Opt Lett*, 25(19):1457-1459. https://doi.org/10.1364/OL.25.001457

Graf J, Hellmann S, Jozwiak C, et al., 2010. Vacuum space charge effect in laser-based solid-state photoemission spectroscopy. *J Appl Phys*, 107(1):014912. https://doi.org/10.1063/1.3273487

Greber T, Raetzo O, Kreutz TJ, et al., 1997. A photoelectron spectrometer for *k*-space mapping above the Fermi level. *Rev Sci Instrum*, 68(12):4549-4554. https://doi.org/10.1063/1.1148429

Grüner F, Becker S, Schramm U, et al., 2007. Design considerations for table-top, laser-based VUV and X-ray free electron lasers. *Appl Phys B*, 86(3):431-435. https://doi.org/10.1007/s00340-006-2565-7

Haight R, Peale DR, 1994. Tunable photoemission with harmonics of subpicosecond lasers. *Rev Sci Instrum*, 65(6): 1853-1857. https://doi.org/10.1063/1.1144834

Haight R, Silberman JA, Lilie MI, 1988. Novel system for picosecond photoemission spectroscopy. *Rev Sci Instrum*, 59(9):1941-1946. https://doi.org/10.1063/1.1140055

Hertz H, 1887. Ueber einen Einfluss des ultravioletten Lichtes auf die electrische Entladung. *Ann Phys*, 267(8):983-1000 (in German). https://doi.org/10.1002/andp.18872670827

Huang LN, McCormick TM, Ochi M, et al., 2016. Spectroscopic evidence for a type II Weyl semimetallic state in $MoTe_2$. *Nat Mater*, 15(11):1155-1160. https://doi.org/10.1038/nmat4685

Hüfner S, 1995. Photoelectron Spectroscopy: Principles and Applications. Springer-Verlag Berlin Heidelberg.

Hüfner S, 2003. Photoelectron Spectroscopy: Principles and Applications (3rd Ed.). Springer-Verlag Berlin Heidelberg.

Jiang R, Mou DX, Wu Y, et al., 2014. Tunable vacuum ultraviolet laser based spectrometer for angle resolved photoemission spectroscopy. *Rev Sci Instrum*, 85(3):033902. https://doi.org/10.1063/1.4867517

Johnson PD, Valla T, Fedorov AV, et al., 2001. Doping and temperature dependence of the mass enhancement observed in the cuprate $Bi_2Sr_2CaCu_2O_{8+\delta}$. *Phys Rev Lett*, 87(17):177007. https://doi.org/10.1103/PhysRevLett.87.177007

Kaminski A, Randeria M, Campuzano JC, et al., 2001. Renormalization of spectral line shape and dispersion below $T_c$ in $Bi_2Sr_2CaCu_2O_{8+\delta}$. *Phys Rev Lett*, 86(6):1070-1073. https://doi.org/10.1103/PhysRevLett.86.1070

Kanai T, Wang XY, Adachi S, et al., 2009. Watt-level tunable deep ultraviolet light source by a KBBF prism-coupled device. *Opt Expr*, 17(10):8696-8703. https://doi.org/10.1364/OE.17.008696

Karlsson HS, Chiaia G, Karlsson UO, 1996. A system for time- and angle-resolved photoelectron spectroscopy based on an amplified femtosecond titanium:sapphire laser system. *Rev Sci Instrum*, 67(10):3610-3615. https://doi.org/10.1063/1.1147067

Kiss T, Kanetaka F, Yokoya T, et al., 2005. Photoemission spectroscopic evidence of gap anisotropy in an *f*-electron superconductor. *Phys Rev Lett*, 94(5):057001. https://doi.org/10.1103/PhysRevLett.94.057001

Kiss T, Shimojima T, Ishizaka K, et al., 2008. A versatile system for ultrahigh resolution, low temperature, and polarization dependent laser-angle-resolved photoemission spectroscopy. *Rev Sci Instrum*, 79(2):023106. https://doi.org/10.1063/1.2839010

Koch P, Bartschke J, L'huillier JA, 2016. High-power actively Q-switched single-mode 1342 nm Nd:$YVO_4$ ring laser, injection-locked by a CW single-frequency microchip laser. *Opt Expr*, 23(24):31357-31366. https://doi.org/10.1364/OE.23.031357

Koralek JD, Douglas JF, Plumb NC, et al., 2006. Laser based angle-resolved photoemission, the sudden approximation, and quasiparticle-like spectral peaks in $Bi_2Sr_2CaCu_2O_{8+\delta}$. *Phys Rev Lett*, 96(1):017005. https://doi.org/10.1103/PhysRevLett.96.017005

Koralek JD, Douglas JF, Plumb NC, et al., 2007. Experimental setup for low-energy laser-based angle resolved photoemission spectroscopy. *Rev Sci Instrum*, 78(5):053905. https://doi.org/10.1063/1.2722413

Lanzara A, Bogdanov PV, Zhou XJ, et al., 2001. Evidence for ubiquitous strong electron–phonon coupling in high-temperature superconductors. *Nature*, 412(6846):510-514. https://doi.org/10.1038/35087518

Li CM, Zhou Y, Zong N, et al., 2009. Sixth harmonic generation of 1064-nm laser in KBBF prism coupling devices under two kinds of gas conditions. *Chin Opt Lett*, 7(7): 621-623.

Li FQ, Zong N, Zhang FF, et al., 2012. Investigation of third-order optical nonlinearity in $KBe_2BO_3F_2$ crystal by Z-scan. *Appl Phys B*, 108(2):301-305. https://doi.org/10.1007/s00340-012-4985-x

Liu GD, Wang GL, Zhu Y, et al., 2008. Development of a vacuum ultraviolet laser-based angle-resolved photoemission system with a superhigh energy resolution better than 1 meV. *Rev Sci Instrum*, 79(2):023105. https://doi.org/10.1063/1.2835901

Lv JH, Wang GL, Xu ZY, et al., 2001. High-efficiency fourth-harmonic generation of KBBF crystal. *Opt Commun*, 200(1-6):415-418. https://doi.org/10.1016/S0030-4018(01)01654-6

Mai ZH, 2013. Synchrotron Radiation Source and Its Application. Science Press, Beijing, China, p.152-620 (in Chinese).

Mårtensson N, Baltzer P, Brühwiler PA, et al., 1994. A very high resolution electron spectrometer. *J Electron Spectrosc Relat Phenom*, 70(2):117-128. https://doi.org/10.1016/0368-2048(94)02224-N

Mathias S, Miaja-Avila L, Murnane MM, et al., 2007. Angle-resolved photoemission spectroscopy with a femtosecond high harmonic light source using a two-dimensional imaging electron analyzer. *Rev Sci Instrum*, 78(8):083105. https://doi.org/10.1063/1.2773783

Nagashima K, Liu LQ, 2001. Phase-matching properties of nonlinear crystals in deep ultraviolet. *Opt Laser Technol*, 33(8):611-615. https://doi.org/10.1016/s0030-3992(01)00084-6

Nakazato T, Ito I, Kobayashi Y, et al., 2016. Phase-matched frequency conversion below 150 nm in $KBe_2BO_3F_2$. *Opt Expr*, 24(15):17149-17158. https://doi.org/10.1364/OE.24.017149

Nessler W, Ogawa S, Nagano H, et al., 1998. Femtosecond time-resolved study of the energy and temperature dependence of hot-electron lifetimes in $Bi_2Sr_2CaCu_2O_{8+\delta}$. *Phys Rev Lett*, 81(20):4480-4483. https://doi.org/10.1103/PhysRevLett.81.4480

Nomura Y, Ito Y, Ozawa A, et al., 2011. Coherent quasi-cw 153 nm light source at 33 MHz repetition rate. *Opt Lett*, 36(10):1758-1760. https://doi.org/10.1364/OL.36.001758

Nordling C, Sokolowski E, Siegbahn K, 1957. Precision method for obtaining absolute values of atomic binding energies. *Phys Rev*, 105(5):1676-1677. https://doi.org/10.1103/PhysRev.105.1676

Passlack S, Mathias S, Andreyev O, et al., 2006. Space charge effects in photoemission with a low repetition, high intensity femtosecond laser source. *J Appl Phys*, 100(2): 024912. https://doi.org/10.1063/1.2217985

Peng QJ, Zong N, Zhang SJ, et al., 2018. DUV/VUV all-solid-state lasers: twenty years of progress and the future. *IEEE J Sel Top Quant Electron*, 24(5):1602312. https://doi.org/10.1109/JSTQE.2018.2829665

Perfetti L, Loukakos PA, Lisowski M, et al., 2006. Time evolution of the electronic structure of 1*T*-$TaS_2$ through the insulator-metal transition. *Phys Rev Lett*, 97(6):067402. https://doi.org/10.1103/PhysRevLett.97.067402

Petersen JC, Kaiser S, Dean N, et al., 2011. Clocking the melting transition of charge and lattice order in 1*T*-$TaS_2$ with ultrafast extreme-ultraviolet angle-resolved photoemission spectroscopy. *Phys Rev Lett*, 107(17):177402. https://doi.org/10.1103/PhysRevLett.107.177402

Petrov V, Rotermund F, Noack F, 1998a. Generation of femtosecond pulses down to 166 nm by sum-frequency mixing in $KB_5O_{8.4}H_2O$. *Electron Lett*, 34(18):1748-1750. https://doi.org/10.1049/el:19981223

Petrov V, Rotermund F, Noack F, et al., 1998b. Vacuum ultraviolet application of $Li_2B_4O_7$ crystals: generation of 100 fs pulses down to 170 nm. *J Appl Phys*, 84(11):5887-5892. https://doi.org/10.1063/1.368904

Reber TJ, Plumb NC, Waugh JA, et al., 2014. Effects, determination, and correction of count rate nonlinearity in multi-channel analog electron detectors. *Rev Sci Instrum*, 85(4):043907. https://doi.org/10.1063/1.4870283

Rohwer T, Hellmann S, Wiesenmayer M, et al., 2011. Collapse of long-range charge order tracked by time-resolved photoemission at high momenta. *Nature*, 471(7339):490-493. https://doi.org/10.1038/nature09829

Shi JR, Tang SJ, Wu B, et al., 2004. Direct extraction of the Eliashberg function for electron-phonon coupling: a case study of Be(1010). *Phys Rev Lett*, 92(18):186401. https://doi.org/10.1103/PhysRevLett.92.186401

Shimojima T, Okazaki K, Shin S, 2015. Low-temperature and high-energy-resolution laser photoemission spectroscopy. *J Phys Soc Jpn*, 84(7):072001. https://doi.org/10.7566/JPSJ.84.072001

Smallwood CL, Zhang WT, Miller TL, et al., 2014. Time- and momentum-resolved gap dynamics in $Bi_2Sr_2CaCu_2O_{8+\delta}$. *Phys Rev B*, 89(11):115126. https://doi.org/10.1103/PhysRevB.89.115126

Smith NV, Traum MM, 1973. Angular dependence of photoemission from the (110) face of GaAs. *Phys Rev Lett*, 31(20):1247-1250. https://doi.org/10.1103/PhysRevLett.31.1247

Smith NV, Traum MM, di Salvo FJ, 1974. Mapping energy bands in layer compounds from the angular dependence of ultraviolet photoemission. *Sol State Commun*, 15(2):211-214. https://doi.org/10.1016/0038-1098(74)90743-1

Sobota JA, Yang SL, Kemper AF, et al., 2013. Direct optical coupling to an unoccupied Dirac surface state in the topological insulator $Bi_2Se_3$. *Phys Rev Lett*, 111(13):136802. https://doi.org/10.1103/PhysRevLett.111.136802

Soluyanov AA, Gresch D, Wang ZJ, et al., 2015. Type-II Weyl semimetals. *Nature*, 527(7579):495-498. https://doi.org/10.1038/nature15768

Taniuchi T, Kotani Y, Shin S, 2015. Ultrahigh-spatial-resolution chemical and magnetic imaging by laser-based photoemission electron microscopy. *Rev Sci Instrum*, 86(2):023701. https://doi.org/10.1063/1.4906755

Trabs P, Noack F, Aleksandrovsky AS, et al., 2016. Generation of coherent radiation in the vacuum ultraviolet using randomly quasi-phase-matched strontium tetraborate. *Opt Lett*, 41(3):618-621. https://doi.org/10.1364/OL.41.000618

Wang CL, Zhang Y, Huang JW, et al., 2017. Evidence of electron-hole imbalance in $WTe_2$ from high-resolution angle-resolved photoemission spectroscopy. *Chin Phys Lett*, 34(9):097305. https://doi.org/10.1088/0256-307X/34/9/097305

Wang GL, Wang XY, Zhou Y, et al., 2008a. 12.95 mW sixth harmonic generation with $KBe_2BO_3F_2$ crystal. *Appl Phys B*, 91(1):95-97. https://doi.org/10.1007/s00340-007-2922-1

Wang GL, Wang XY, Zhou Y, et al., 2008b. High-efficiency frequency conversion in deep ultraviolet with a $KBe_2BO_3F_2$ prism-coupled device. *Appl Opt*, 47(3):486-488. https://doi.org/10.1364/AO.47.000486

Wang YH, Steinberg H, Jarillo-Herrero P, et al., 2013. Observation of Floquet-Bloch states on the surface of a topological insulator. *Science*, 342(6157):453-457. https://doi.org/10.1126/science.1239834

Wang ZM, Zhang JY, Yang F, et al., 2009. Stable operation of 4 mW nanoseconds radiation at 177.3 nm by second harmonic generation in $KBe_2BO_3F_2$ crystals. *Opt Expr*, 17(22):20021-20032. https://doi.org/10.1364/OE.17.020021

Won R, 2014. Two-dimensional materials: laser Q-switching. *Nat Photon*, 8(6):422. https://doi.org/10.1038/nphoton.2014.123

Wu Y, Mou DX, Jo NH, et al., 2016. Observation of Fermi arcs in the type-II Weyl semimetal candidate $WTe_2$. *Phys Rev B*, 94(12):121113. https://doi.org/10.1103/PhysRevB.94.121113

Xie ZJ, He SL, Chen CY, et al., 2014. Orbital-selective spin texture and its manipulation in a topological insulator. *Nat Commun*, 5:3382. https://doi.org/10.1038/ncomms4382

Xu B, Liu LJ, Wang XY, et al., 2015. Generation of high power 200 mW laser radiation at 177.3 nm in $KBe_2BO_3F_2$ crystal. *Appl Phys B*, 121(4):489-494. https://doi.org/10.1007/s00340-015-6260-4

Xu M, Ermolenkov VV, Uversky VN, et al., 2008. Hen egg white lysozyme fibrillation: a deep-UV resonance Raman spectroscopic study. *J Biophoton*, 1(3):215-229. https://doi.org/10.1002/jbio.200710013

Xu Z, Zhang FF, Zhang SJ, et al., 2014a. Experimental investigation and theoretical analysis of pulse repetition rate adjustable deep ultraviolet picosecond radiation by second harmonic generation in $KBe_2BO_3F_2$. *Laser Phys*, 24(6):065401. https://doi.org/10.1088/1054-660X/24/6/065401

Xu Z, Tu W, Yang F, et al., 2014b. Narrow linewidth 177.3-nm nanosecond laser with high efficiency and high power. *IEEE Photon Technol Lett*, 26(10):980-982. https://doi.org/10.1109/LPT.2014.2311091

Xu ZY, Lü JH, Wang GL, et al., 2001. Non-linear Optical Crystal Laser Frequency Variable Grating Coupler. Chinese Patent No. CN01123553.5 (in Chinese).

Yang F, Wang Z, Zhou Y, et al., 2009. Theoretical and experimental investigations of nanosecond 177.3 nm deep-

ultraviolet light by second harmonic generation in KBBF. *Appl Phys B*, 96(2-3):415-422. https://doi.org/10.1007/s00340-009-3506-z

Yang F, Wang ZM, Zhou Y, et al., 2010. 41 mW high average power picosecond 177.3 nm laser by second-harmonic generation in KBBF. *Opt Commun*, 283(1):142-145. https://doi.org/10.1016/j.optcom.2009.09.051

Yang J, Yang F, Zhang JY, et al., 2013. Pulse broadening of deep ultraviolet femtosecond laser from second harmonic generation in $KBe_2BO_3F_2$ crystal. *Opt Commun*, 288: 114-117. https://doi.org/10.1016/j.optcom.2012.09.054

Zhang FF, Yang F, Zhang SJ, et al., 2012. A polarization-adjustable picosecond deep-ultraviolet laser for spin- and angle-resolved photoemission spectroscopy. *Chin Phys Lett*, 29(6):064206. https://doi.org/10.1088/0256-307X/29/6/064206

Zhang FF, Yang F, Zhang SJ, et al., 2013. Picosecond widely tunable deep-ultraviolet laser for angle-resolved photoemission spectroscopy. *Chin Phys B*, 22(6):064212. https://doi.org/10.1088/1674-1056/22/6/064212

Zhang HJ, Wang G, Guo L, et al., 2008. 175 to 210 nm widely tunable deep-ultraviolet light generation based on KBBF crystal. *Appl Phys B*, 93(2-3):323-326. https://doi.org/10.1007/s00340-008-3198-9

Zhang HJ, Liu CX, Zhang SC, 2013. Spin-orbital texture in topological insulators. *Phys Rev Lett*, 111(6):066801. https://doi.org/10.1103/PhysRevLett.111.066801

Zhang SJ, Cui DF, Zhang FF, et al., 2014. High power all solid state VUV lasers. *J Electron Spectrosc Relat Phenom*, 196:20-23. https://doi.org/10.1016/j.elspec.2014.01.018

Zhang WT, Liu GD, Meng JQ, et al., 2008. High energy dispersion relations for the high temperature $Bi_2Sr_2CaCu_2O_8$ superconductor from laser-based angle-resolved photoemission spectroscopy. *Phys Rev Lett*, 101(1):017002. https://doi.org/10.1103/PhysRevLett.101.017002

Zhang WT, Smallwood CL, Jozwiak C, et al., 2013. Signatures of superconductivity and pseudogap formation in non-equilibrium nodal quasiparticles revealed by ultrafast angle-resolved photoemission. *Phys Rev B*, 88(24): 245132. https://doi.org/10.1103/PhysRevB.88.245132

Zhang X, Wang ZM, Wang GL, et al., 2009. Widely tunable and high-average-power fourth-harmonic generation of a Ti:sapphire laser with a $KBe_2BO_3F_2$ prism-coupled device. *Opt Lett*, 34(9):1342-1344. https://doi.org/10.1364/OL.34.001342

Zhang X, Wang ZM, Luo SY, et al., 2011. Widely tunable fourth harmonic generation of a Ti:sapphire laser based on RBBF crystal. *Appl Phys B*, 102(4):825-830. https://doi.org/10.1007/s00340-011-4370-1

Zhang Y, Sato Y, Watanabe N, et al., 2009. Generation of quasi-continuous-wave vacuum-ultraviolet coherent light by fourth-harmonic of a Ti:sapphire laser with KBBF crystal. *Opt Expr*, 17(10):8119-8124. https://doi.org/10.1364/OE.17.008119

Zhang Y, Wang CL, Yu L, et al., 2017. Electronic evidence of temperature-induced Lifshitz transition and topological nature in $ZrTe_5$. *Nat Commun*, 8:15512. https://doi.org/10.1038/ncomms15512

Zhou C, Kanai T, Wang XY, et al., 2012. Generation of ultrashort 25-μJ pulses at 200 nm by dual broadband frequency doubling with a thin $KBe_2BO_3F_2$ crystal. *Opt Expr*, 20(13):13684-13691. https://doi.org/10.1364/OE.20.013684

Zhou XJ, Yoshida T, Lanzara A, et al., 2003. High-temperature superconductors: universal nodal Fermi velocity. *Nature*, 423(6938):398. https://doi.org/10.1038/423398a

Zhou XJ, He SL, Liu GD, et al., 2018. New developments in laser-based photoemission spectroscopy and its scientific applications: a key issues review. *Rep Prog Phys*, 81(6): 062101. https://doi.org/10.1088/1361-6633/aab0cc

Zhou Y, Wang GL, Li CM, et al., 2008. Sixth harmonic of a Nd:$YVO_4$ laser generation in KBBF for ARPES. *Chin Phys Lett*, 25(3):963-965. https://doi.org/10.1088/0256-307X/25/3/043